

# **Groundwater-Gossan Interaction and the Genesis of the Secondary Siderite at Las Cruces Ore Deposit (SW Spain)**

## **ABSTRACT**

The Las Cruces secondary siderite deposit has sparked an interest in the scientific community because of its unique mineralogy. The original gossan formed by goethite and hematite has been replaced by a siderite and galena rock. We postulate that this rock can be formed by the interaction of iron oxides with groundwater similar in composition to that of the present day,. Hydrochemical and isotopic characteristics of groundwater support this hypothesis. The negative Eh values, the existence of H<sub>2</sub>S and the tendency toward high sulfate isotope values indicate a reducing groundwater condition. The high ammonium, boron and iodine concentrations as well as the low  $\delta^{13}\text{C}$  values of dissolved inorganic carbon (DIC) confirm the organic matter degradation. The reductive dissolution of Pb-bearing goethite at the expense of DOC leads to the precipitation of Fe-sulfides, galena and siderite. The formation of siderite from this process is confirmed by the low amount of dissolved Fe in groundwater (<10 ppb), its low  $\delta^{13}\text{C}$  values and thermodynamic calculations. One-dimensional reactive transport modeling demonstrated that the present-day groundwater flux and composition could form the siderite rock in less than 1 Ma with no external supply of reactants. Sensitivity analyses revealed that the time of formation depends on the structure of the groundwater flux (spaced fractures or pervasive), the flow rate and especially the DOC concentration. In fact, calculations with the highest DOC measured concentration resulted in a mineral zonation formed by Fe-sulfides and siderite, with galena in both zones, that agrees with the observations. Reactive transport calculations and the similarity of its high  $\delta^{34}\text{S}$  values indicate that the sulfur of galena came from the current groundwater.

## 27 1. INTRODUCTION

28 The weathering profile developed in the Volcanogenic Host Massive Sulfide (VHMS) has been  
29 extensively studied worldwide in terms of composition, structure and genesis (Crawford et al.,  
30 1992; Doyle and Allen, 2003; Galley et al., 2007; Large, 1992). The formation and  
31 characteristics of this profile depend on such factors as rock host type, climate, relief, sulfide  
32 paragenesis, groundwater level, pH, and Eh. However, a common weathering profile can be  
33 defined in three differentiated zones: primary, cementation and oxidation zones (Nickel, 1984;  
34 Scott et al., 2001b; Thornber and Wildman, 1984). The upper part of the oxidation zone is  
35 known as “gossan”. The gossan is formed mainly by oxides and oxyhydroxides of Fe as  
36 goethite and hematite with jarosite in minor proportion. This typical gossan mineralogy is found  
37 in most worldwide deposits, for example in the Australian Woodlawn and Currawong mine  
38 (Scott et al., 2001a), in deposits from the Spanish-Portuguese Iberian Pyritic Belt (IPB)  
39 (Almodóvar et al., 1997; Kosakevitch et al., 1993; De Oliveira et al., 2011; Velasco et al., 2013;  
40 Viñals et al., 1995), or in the Flambeau mine in the U.S. (Ross, 1997). ( ).

41 The IPB, with over 1.600 million tonnes of massive sulfides, is one of the most important  
42 metallogenic provinces in the world. The IPB integrates more than 100 mines, most of them  
43 inactive, and represents 22% of worldwide VHMS deposits (Tornos, 2006). The IPB has been  
44 extensively studied based on genesis, structure, mineralogy, and petrology (Leistel et al., 1997;  
45 Marcoux, 1997; Sáez et al., 1996; Strauss and Madel, 1974; Tornos et al., 2000). Most gossans  
46 of the IPB are in the present-day surface except for those of Las Cruces in SW Spain and the  
47 Lagoa Salgada in Portugal, which are covered by Cenozoic sediments. The Las Cruces  
48 cementation zone presents an exceptional wealth in copper, with 6.2% Cu grade and initial  
49 reserves of 17.6 Mt. Moreover, the deposit has important resources of 2 Mt of gossan with 4.5%  
50 lead, 5% g/t gold and 115 g/t silver in the supergene profile (Yesares et al., 2014a). The Las  
51 Cruces secondary deposit has also sparked an interest in the scientific community because of the  
52 uniqueness of its mineralogical composition (Blake, 2008; Capitán Suárez, 2006; Knight, 2000;

Miguélez et al., 2011; Miguelez et al., 2011; Moreno C., 2003; Tornos et al., 2014; Yesares et al., 2014a). The mineralogy is formed mainly by siderite with galena, calcite, goethite, hematite and precious metals. A comparable case has only been reported in the South Urals (Belogub et al., 2003). The genesis of this mineralogy is the subject of controversy and several hypotheses have been proposed. Knight (2000) considers that the secondary enrichment was multi-genetic and related to events ranging from alteration by a seawater hydrothermal system during primary deposition (Carboniferous) to post-Tertiary weathering. Blake (2008) proposed that fluctuating oxidizing and reducing conditions, coupled with biogenic processes in groundwater, provided a suitable mechanism for the formation of the secondary deposit composition. Tornos et al. (2014) suggested that anaerobic microbial activity was responsible for the uncommon mineralogy of the Las Cruces secondary deposit and proposed that siderite is formed in a natural bioreactor where microbial sulfate reduction was coupled to methane oxidation. These post-Miocene processes occurred below a thick impermeable marl unit from Cenozoic Guadalquivir basin deposits. Conversely, Capitán Suárez (2006) proposed for the Las Cruces gossan an evolution controlled by the Miocene transgressive–regressive episodes affecting the area. Yesares et al. (2014) proposed that the formation of the secondary deposit was related to the circulation of surficial waters flowing downwards the Cenozoic sediments.

The main objective of this paper is to quantitatively discuss the feasibility of a genetic model of the Las Cruces siderite rock resulting from the interaction of a previous gossan with groundwater similar to present day composition. To reach this objective, it was necessary to 1) characterize the hydrochemistry and isotopes of present day groundwater, 2) quantify the groundwater flow rate through the gossan by performing a hydrogeological numerical model, and 3) quantify the biogeochemical interaction of groundwater flow through the gossan rocks by reactive transport numerical modeling.

## **2. SITE DESCRIPTION**

### **2.1. Geological setting**

The Las Cruces ore deposit is located at the eastern edge of the Iberian Pyritic Belt (IPB), approximately 20 km North of Seville. The IPB is a metallogenic province 250 km long and 30-50 km wide, extending from south of Lisbon (Portugal) to Seville (Spain) (Figure 1A). It contains half of the worldwide giant volcanogenic massive sulfide deposits and has been extensively described. The IPB shows a stratigraphic succession formed by upper Paleozoic sedimentary marine materials and volcanic rocks (Schermerhorn, 1971; Moreno and Sáez, 1990; Pascual et al., 1994). These materials were affected by several tectonic phases during the Variscan orogeny resulting in NW-SE to W-E structures and a low grade metamorphism, (Quesada, 1991; Silva et al., 1990). Later, the Alpine orogeny played an important role, reactivating the structures previously formed. The exhumation of the Variscan chain exposed the massive sulfide deposits to the surface, thus promoting oxidation and the formation of gossans. Part of the IPB was covered by Cenozoic marine materials that refilled the Guadalquivir basin because of marine transgression-regression (Abad de los Santos, 2007). The dominant materials are bioclastic calcarenites related to shallow marine environments and marls related to deep marine environments.

The study area is formed by a Paleozoic basement composed of black shales and volcanic rock sequences, outcropping to the north of the area coinciding with higher topography. The Paleozoic is overlain by two Cenozoic formations: the Niebla and Gibráleon formations (Fm.). The Niebla Fm. is composed of basal conglomerates (bioclastic calcarenites) and sandstones rich in marine micro/macro fauna. The Gibráleon Fm. is formed by marine bluish marls rich in organic matter (Figure 1B and C). All these materials are affected by Alpine faults with a main SW-NE and a secondary NW-SE orientation (Figure 1B).

Based on the age of river terraces in the region, it is considered that the geomorphological and hydraulic (and therefore hydrogeological) functioning of the study area have not changed significantly from low-Pleistocene (1,8 Ma) to recent times (Escudero, 1994; Moral et al., 2013; Salvany et al., 2001)

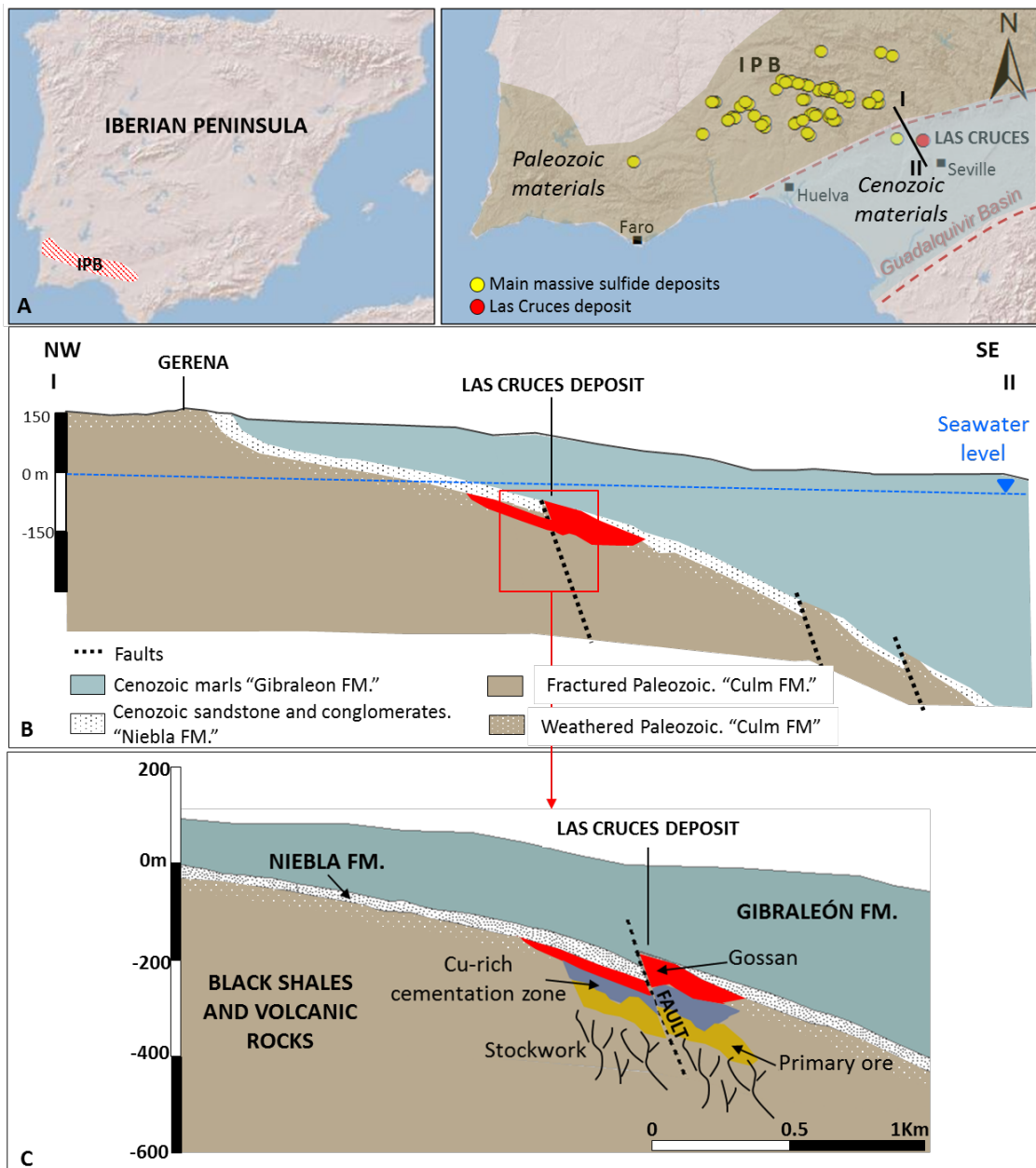


Figure 1. A) Location of the Iberian Pyrite Belt (IPB) and the Las Cruces deposit. B) Section showing the main geological trends and C) the weathering profile of Las Cruces deposit.

## 2.2. Ore deposit description

The Las Cruces ore deposit is a sulfide massive body enclosed in Paleozoic materials. The deposit was exhumed in Miocene time and the Paleozoic rocks and the massive sulfides were weathered under atmospheric conditions. Consequently, a supergene profile was developed in the upper part of the sulfide massive composed of the primary zone, cementation zone and oxidation zone (Figure 1C). The profile alteration remains intact because it was buried by

Cenozoic sediments during the Tortonian marine transgression. The secondary deposit of Las Cruces has a peculiarity in its composition where the original gossan formed by goethite and hematite have been replaced by siderite, galena and iron metastable sulfides such as greigite and smythite (Tornos et al., 2014).

The primary zone, of the Las Cruces deposit, is formed by unaltered sulfides and integrates a sulfide massive body and stockwork mineralization. The main minerals in the massive body are pyrite, chalcopyrite, sphalerite and galena, whereas the stockwork is made up of pyrite and chalcopyrite, similar to other sulfide massive deposits from the IPB (García de Miguel, 1990; Marcoux et al., 1996). The cementation zone is an enrichment in chalcocite. Tornos et al. (2016) differentiated 2 zones in the secondary deposit: (1) a basal “Black rock” formed mainly by iron sulfides, galena, calcite and quartz and (2) a “Red rock” formed mostly by siderite, galena and residual goethite, which constitutes most of the volume. Mineralogical details and textural features are described in Yesares et al. (2015), who described textures of replacement of Fe-oxyhydroxides by siderite and sulfides.

Some isotopic studies have reported data about the Las Cruces ore deposit and have helped to improve the understanding of the formation of this deposit. For example,  $\delta^{13}\text{C}$  values of the siderite were provided by Capitán Suárez (2006) and Tornos et al. (2014) and ranged from -47.95 to -13.4‰ and -41.7 to -17.6‰, respectively. Capitán Suárez (2006) interpreted these values as linked to biomass and concluded that the low values indicated a soil-related origin. However, Tornos et al. (2014) proposed that these values can only be derived by biologically mediated methanotrophy or anaerobic oxidation of methane (AOM) or of low molecular weight organic compounds. Moreover, Knight (2000) and Tornos et al. (2014) presented  $\delta^{34}\text{S}$  values for both primary and secondary mineralization, which will be discussed below.

### **2.3. Aqueous phase characterization**

The conglomerate and sand strata of the Niebla formation, together with a narrow layer of weathered Paleozoic basement, constitutes an aquifer. The upper part of fractured Paleozoic basement also constitutes a zone of moderate permeability. These aquifers outcrop to the north

of the study area, constituting the recharge zone. The Niebla Fm. dips southward and is confined by the overlying marls of the Gibrleon Fm. that reaches a thickness of hundreds of metres (Figure 2A). Five zones can be differentiated based on their transmissivity values: (1) corresponds to the marls of the Gibrleon Fm.; (2) the sands and conglomerates of Niebla formation; (3) the weathered part of upper Paleozoic formation; (4) the Paleozoic rocks; and (5) the faults (Figure 2A). The approximately 10- to 30-m-thick Niebla Fm. has transmissivity values that range between 10 and 500 m<sup>2</sup>/d, and its storage coefficient values are on the order of 10<sup>-2</sup> within the unconfined zone and between 10<sup>-3</sup> and 10<sup>-5</sup> in the confined areas (CHG, 2012). It is sealed near the recharge zone by the low transmissivity (<5 m<sup>2</sup>/d) marls of the Gibrleon Fm. (CHG, 2012). No previous values have been measured for the Paleozoic, the weathered Paleozoic and the main faults. Following the groundwater head inventory and prior to mine operations, groundwater regional flow was dominantly from the northwest to the southeast (Figure 2B). There was an abnormal change of gradient in the area around the mine site attributed to an elevation of the basement paleorelief, where the Niebla Fm. disappears and the marl layer rests directly on the Paleozoic (Figure 2A and B). The main recharge of the aquifer is by rainwater infiltration in the outcropping zone (NW). The groundwater residence time, estimated from <sup>3</sup>H, <sup>14</sup>C and <sup>36</sup>Cl analyses, confirms the existence of some recharge of the Niebla aquifer from the underlying Paleozoic. A residence time up to 30.000 years was obtained for the groundwater close to the Las Cruces deposit (Scheiber et al., 2015). The total estimated annual recharge is 32 hm<sup>3</sup> (25 mm/y) for an area of 1,300 km<sup>2</sup>. The discharge was 34 hm<sup>3</sup>/y and corresponds to agricultural and consumption extractions (CHG, 2012; Navarro et al., 1993). Note that the Niebla aquifer was artesian south of the outcropping area prior to mining and agricultural extractions (IGME, 1984). Another important fact is the role of the main fault system as a possible discharge zone. Several data items, such as high groundwater temperatures (up to 37.5 °C) detected in areas near faults, confirm the presence of upward flows along these faults.

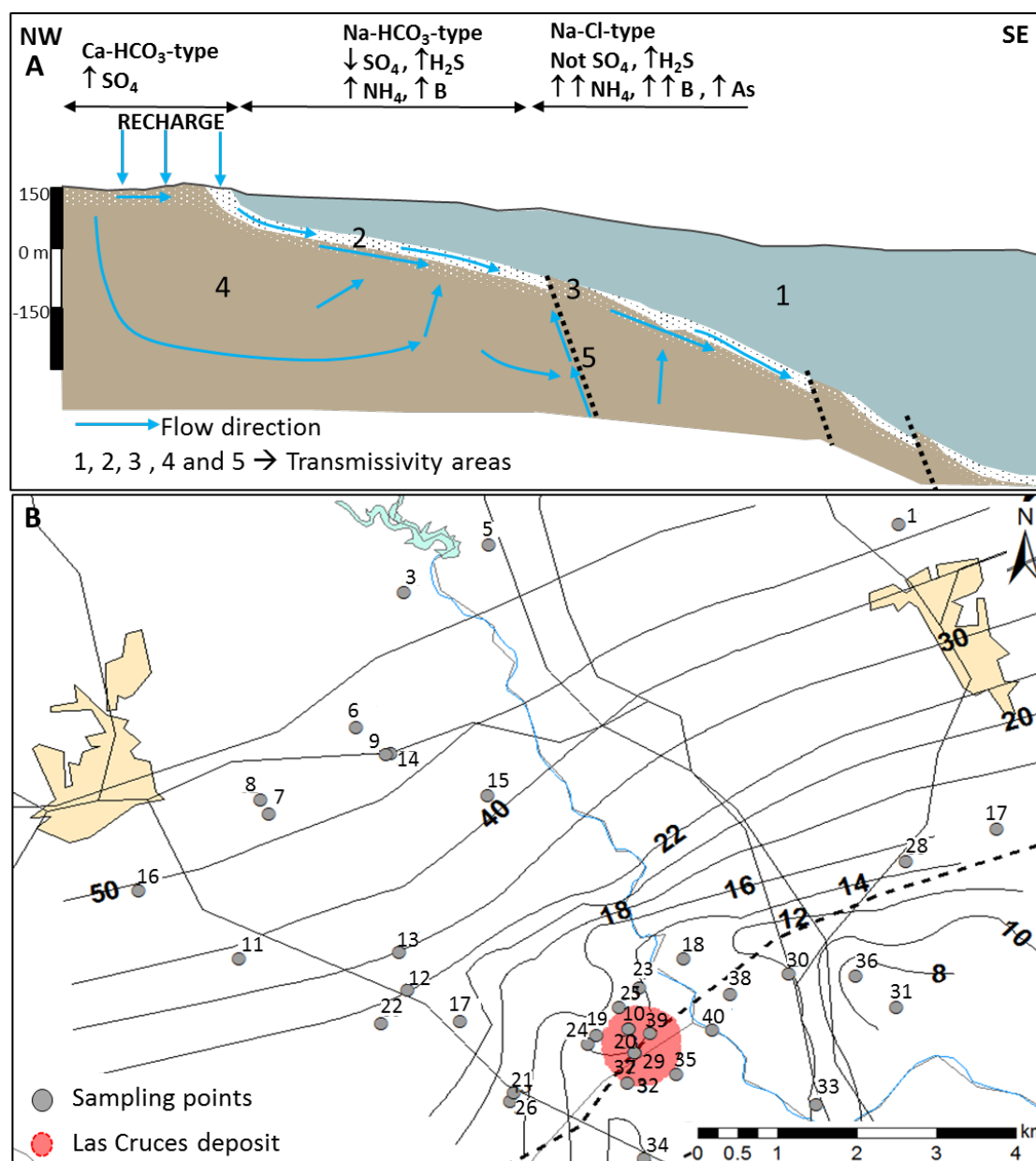


Figure 2. A) Simplified hydrogeological cross-section and hydrochemical characteristics of groundwater; B) Piezometric map of study area and sampling points distribution; The lines and bold labels are the interpolated groundwater isopotential lines and heads in masl (meters above sea level).

## 2.4. Hydrogeochemical setting

The groundwater chemistry was detailed by Scheiber et al. (2016) and is summarized below. Groundwater shows an evolution along flow lines from the NW to SE direction (Figure 2A and B). Groundwater is of the Ca-HCO<sub>3</sub>-type initially, switching to Na-HCO<sub>3</sub>- and Na-Cl-type downstream in proximity to the recharge zone. An excess in Na concentrations with respect to seawater ratios is observed towards deeper portions of the aquifer related to a Na-Ca exchange

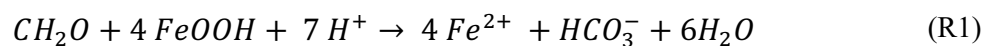


process that occurs within dispersed clay layers in the aquifer or within the overlying formation. There is also an increase in pH and specific conductivity (SC) and a decrease of Eh values downstream. In proximity to the Las Cruces ore, the groundwater has basic pH values up to 10.6 (Figure 3A), the SC reaches values from 1000 up to 5.940  $\mu\text{S}\cdot\text{cm}^{-1}$ . Dissolved Organic Carbon (DOC) concentration ranges from 2.86 up to 15.9  $\text{mg}\cdot\text{L}^{-1}$  in the deepest area (Figure 3B). These values are above the typical values in groundwater of  $<1 \text{ mg}\cdot\text{L}^{-1}$  (Kalbitz et al., 2000). Complete analyses can be found in Supplementary Information (Table A1).

The negative Eh values (Figure 3A), together with the decreasing sulfate concentration and the presence of  $\text{H}_2\text{S}$ , suggest that this is an environment with reducing conditions. Values of  $\delta^{34}\text{S}$  and  $\delta^{18}\text{O}$  of the sulfate molecule range between -17.2 to 20.4‰ (CDT), and 1.9 to 18.1‰ (V-SMOW), respectively, for samples near the mining site. This tendency towards higher  $\delta^{18}\text{O}$  and  $\delta^{34}\text{S}$  values confirms the sulfate reduction shown in Figure 4.

Moreover, high ammonium (up to 12.8  $\text{mg}\cdot\text{L}^{-1}$ ), boron (up to 3.48  $\text{mg}\cdot\text{L}^{-1}$ ) and iodide (up to 0.67  $\text{mg}\cdot\text{L}^{-1}$ ) concentrations are found in parts of the deep Niebla and Paleozoic aquifers (Figure 3C) and increase towards the deepest areas close to the ore body. The high  $\text{NH}_4$ , B and I concentrations have been attributed to the anoxic decomposition of marine organic matter (Whitehead, 1974; Goldberg et al., 1993; Scheiber et al., 2016). Moreover, the  $\delta^{13}\text{C}$  values of dissolved inorganic carbon (DIC) are approximately -10‰ in the ore proximity. All these facts indicate that the organic matter occurs along a groundwater flow path.

From the groundwater characteristics described above, we can postulate that the current groundwater can induce the reductive dissolution of the goethite at the expense of DOC (represented as  $\text{CH}_2\text{O}$ ). The reaction increased the pH and released  $\text{Fe}^{2+}$  and  $\text{HCO}_3^-$ , which promoted siderite precipitation by the following reaction:



Arsenic concentration, present as As(III), ranging from below the limit detection to 0.18 mg/L has also been found locally in some wells from the deepest Niebla aquifer. The presence of As(III) also suggests the dissolution of the As-bearing goethite in a reducing environment. The

low amount of Fe (< 10 ppb) detected in groundwater can be due to siderite precipitation. Indeed, thermodynamic calculations performed with PHREEQC and the Wateq4 database (Parkhurst and Appelo, 2013) indicate that groundwater close to the ore body is supersaturated and very close to equilibrium with respect to siderite (Figure 3D).

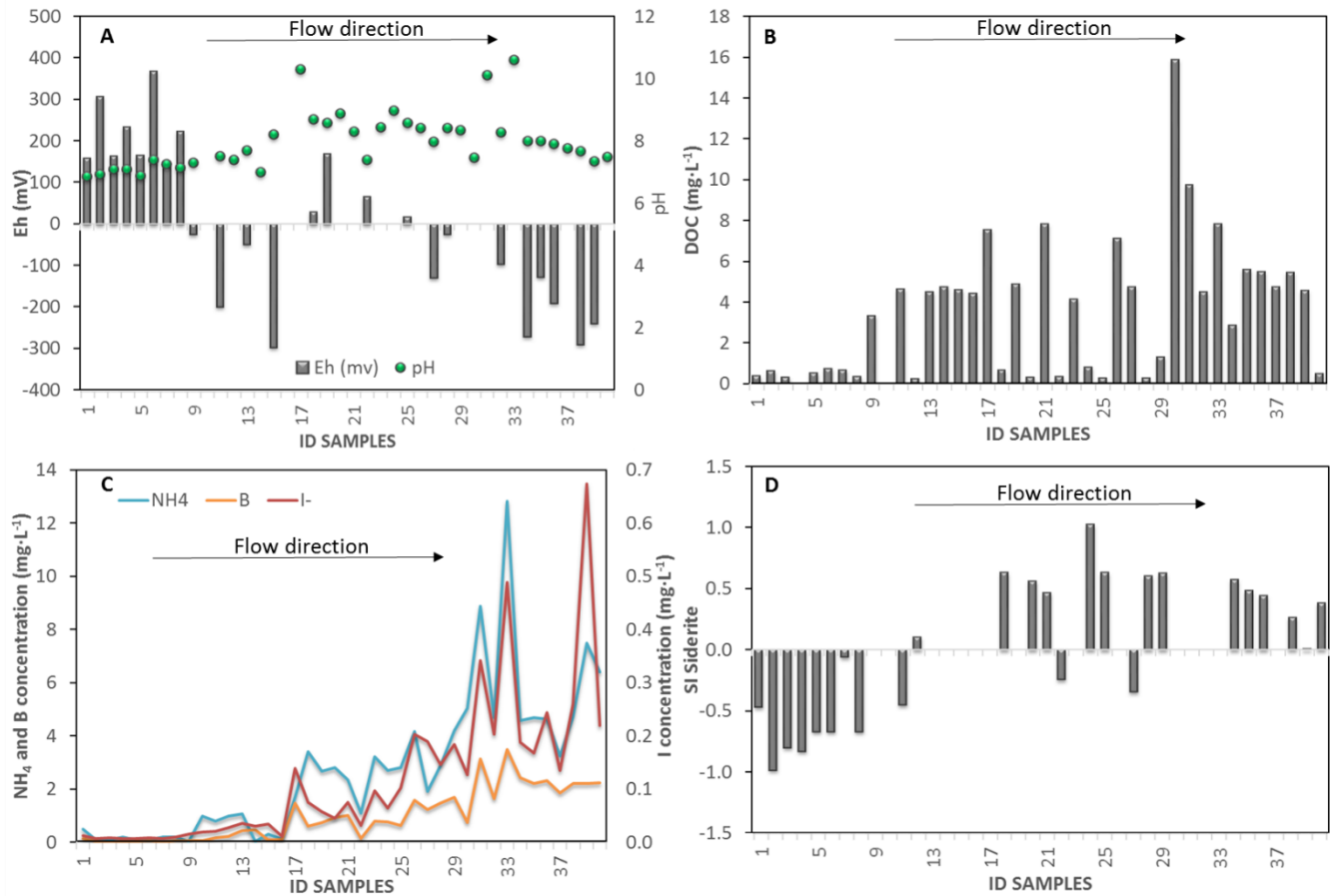


**Figure 3. (A) Eh and pH values of groundwater; (B) Dissolved Organic Carbon concentration of groundwater; (C) NH<sub>4</sub>, B and I concentration and (D) Saturation index of siderite. The location of the samples is shown in Figure 2B.**

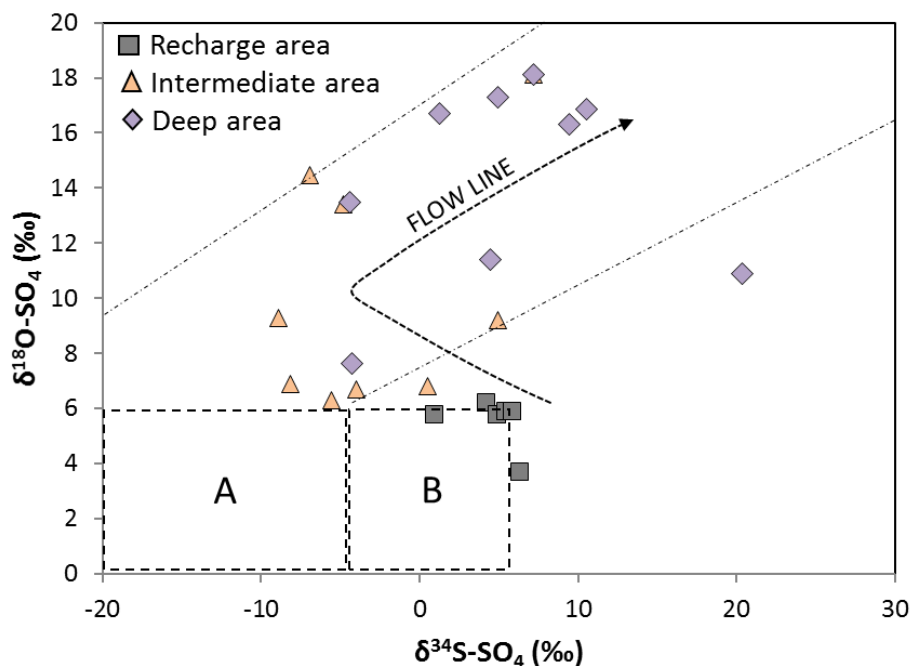


**Figure 4. Representation of the isotopic content of sulfates in groundwater. Legend: (A) Sulfate derived from sedimentary, (B) Sulfate derived from magmatic sulfide. Figure modified from Scheiber et al. (2015)**

## 2.5. Solid phase characterization

Another aspect to consider is that groundwater transports a very low content of Pb (< 1 ppb) and thus an additional source of the element to form galena is assumed to be present in the initial gossan. Minerals from the jarosite family rich in lead, such as plumbojarosite or beudantite, have very often been described as the mineral limiting the low Pb concentrations of massive sulfide oxidation sites, particularly in the Iberian Pyrite Belt (Figueiredo and Pereira da Silva, 2011; Nieto et al., 2003). However, these minerals have not been identified in the oxides remaining in the Las Cruces siderite rock.

To determine the origin of Pb, three samples rich in goethite were analysed by Electron microprobe (EPM). Lead, As, Cu, Fe, S and Sb in goethite were quantified (Figure 5 and 6). The complete analyses are shown in Table A2 of Supplementary Information.

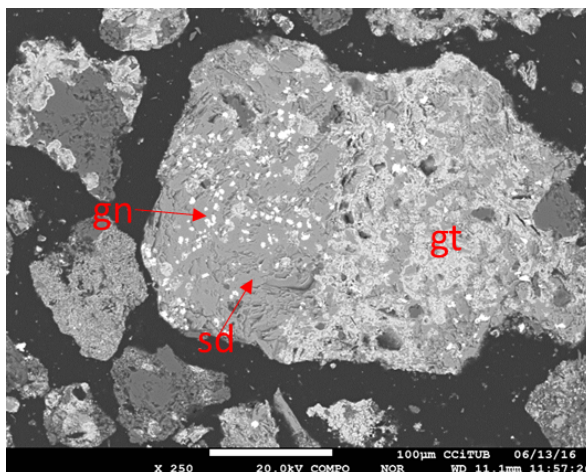


**Figure 5. Electron microprobe images of secondary deposit fragments. Goethite (gt) replaced by siderite (sd) and galena (gn).**

The EPM analyses in goethite suggest that this mineral is the main source of Pb and Sb that subsequently form galena and Pb-sulfosalts and for As found in groundwater in some wells from the deep zone.

GOETHITE	
No. Of data=53	Average±Standard deviation
As <sub>2</sub> O <sub>5</sub>	0.387±0.15
Fe <sub>2</sub> O <sub>3</sub>	93.304±1.27
PbO	0.946±0.14
SO <sub>3</sub>	0.364±0.07
Sb <sub>2</sub> O <sub>5</sub>	0.209±0.12

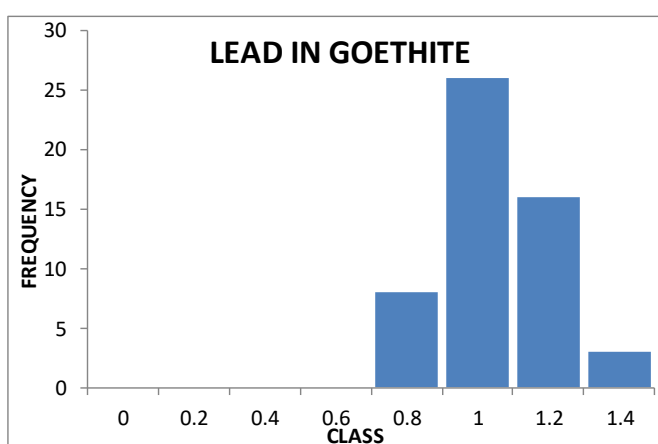


**Figure 6. Results from electron microprobe analyses of goethite (N= 53) and histogram of the frequency of lead in goethite.**

The presence of As, Pb and Sb in goethite has been extensively described. Fe-oxyhydroxides are characterized by a very high specific surface area of  $\pm 300 \text{ m}^2 \cdot \text{g}^{-1}$  and a high adsorption capacity capable of adsorbing large amounts of metals and metalloids (Davis and Leckie, 1978). Many studies related to As adsorption on goethite are available (Bowell, 1994; Dixit and Hering, 2003; Fendorf et al., 1997; Goldberg and Johnston, 2001). Lead adsorption on goethite was investigated by Forbes et al. (1976), Hiemstra and Van Riemsdijk (1999), Coughlin and Stone (1995), and Bargar et al. (1997), among others. Several studies have also investigated the

Sb adsorption mechanism on Fe-oxyhydroxides by laboratory experiments (Leuz et al., 2006; Tighe et al., 2005). No mineral phases other than goethite have been identified by X ray Diffraction, but the atomic Pb/S ratio close to 1 (0.96) and the narrow dispersion of the Pb and S contents suggest that these elements could be present as nanoinclusions of a Pb:S 1:1 phase anglesite homogeneously distributed in goethite.

Additionally, sulfur isotope data provide valuable information about the environmental conditions of ore formation and the sources of sulfur. Our values fall between the range reported by Knight (2000) and Tornos et al. (2016) for galena from the Las Cruces deposit and significantly higher than the values reported for other sulfides from the IPB (Table 1). The similarity between the  $\delta^{34}\text{S}$  values of the secondary mineralization of the Las Cruces deposit and those of groundwater sulfate suggests that the current galena composition can be explained by the groundwater and gossan interaction. Indeed, the sulfate reduction increases the  $\delta^{34}\text{S}_{\text{SO}_4}$  of groundwater along its transit through the aquifer. The remaining  $\delta^{34}\text{S}_{\text{SO}_4}$  values of groundwater from the deep zone close to the Las Cruces deposit are as high as 10‰ and up to 20‰ (Figure 4). The complete reduction of  $\text{SO}_4$  and the precipitation of galena can produce a solid with high  $\delta^{34}\text{S}$  values. Therefore, the  $\delta^{34}\text{S}_{\text{SO}_4}$  data suggest a high influence of the S carried by groundwater in the final galena sulfur. Since galena would have remained stable under reducing conditions, initial microinclusions in goethite would probably be of a oxidized phase such as anglesite or beudantite.

RE DEPOSIT	$\delta^{34}\text{S}$ MIN. VALUE	$\delta^{34}\text{S}$ MAX. VALUE (‰)	DATA SOURCE
Agua Teñidas	-5.6	+3.6	Velasco et al. (1998)
Aljustrel	-20.4	+4.0	
Aznalcollar	-6.0	+4.4	
Concepción	-1.4	+9.2	
Cueva de la Mora	+2.5	+7.1	
La Zarza	-7.3	+7.8	
Lousal	-8.3	+5.5	
Monte Romero	+3.3	+9.0	
Neves Corvo	-11.1	+6.0	
Rio Tinto	-14.1	+12.4	
San Miguel	-3.9	+9.2	
Sotiel	-34.2	+6.7	

Tharsis	-26.8	+3.5	
Aznalcollar	-6.0	+4.4	Almodóvar et al. (1997)
Tharsis	-10.7	+3.5	Kase et al. (1990)
Tharsis	-11.5	+0.0	Tornos et al. (1998)
<b>Las Cruces secondary deposit</b>	<b>+11.9</b>	<b>+25.9</b>	<b>Tornos et al. (2014)</b>
<b>Las Cruces secondary deposit</b>	<b>+3.5</b>	<b>+21.7</b>	<b>Knight (2000)</b>
<b>Las Cruces secondary deposit</b>	<b>+10.2</b>	<b>+13.5</b>	<b>This work.</b>

Table 1. Summary of sulfur isotope data of some massive sulfide deposits from the Iberian Pyrite Belt

### 3. QUANTITATIVE MODELING AND DISCUSSION

#### 3.1. Numerical flow model

The main purpose of quantitative modeling was to apply a semi-quantitative approach to the flow recently circulating through the original gossan. The flow rate value obtained was used to perform reactive transport modeling. To achieve this purpose, a 2D numerical flow model in steady conditions based on piezometric data prior to mining activity was applied. The TRANSIN code (Medina and Carrera, 2003) was used for the modeling process using its graphical interface VISUAL TRANSIN (UPC (2003), <http://h2ogeo.upc.edu/en/investigation-hydrogeology/software>). The model corresponds to a NW-SE vertical section 25 km in length and 1.2 km thick. Based on the data described in the preceding sections, the following boundary conditions were imposed: (C1) prescribed head in SE boundary; (C2) prescribed recharge in the Paleozoic outcrop ( $1.2 \text{ m}^3\text{y}^{-1}$ , CHG (2012)) and (C3) in the Niebla formation outcrop ( $0.3 \text{ m}^3\text{y}^{-1}$ , CHG (2012)); and (C4) mixed conditions representing the artesian zone in the marls surface close to the recharge area (IGME, 1984). The model was discretized in the five transmissivity zones based on the geologic differences defined in section 2.4: the Gibrleón Fm. (T1), the Niebla Fm. (T2), the weathered Paleozoic (T3), Paleozoic schists and volcanics (T4) and faults (T5) (Figure 2A).

TRANSIN solves the flow equation by applying the finite element method and the inverse problem using automatic calibration. A finite element mesh of 4752 nodes and 8947 triangular elements was built. The model calibration was performed by fitting the measured and calculated groundwater levels, the hydraulic parameters applied and their uncertainty range and the mass balance consistency. The transmissivity data from the CHG (2012) and the piezometric levels

from previous mining activity (Figure 2B) were used in the calibration process. The starting and calibrated values of transmissivity and recharge are listed in Table 2.

ZONE	DESCRIPTION	TRANSMISSIVITY m <sup>2</sup> d <sup>-1</sup>	
		Reference	Calibrate
T1	Gibraleon Fm.	<5	0.2
T2	Niebla Fm.	10-500	20
T3	Weathered Paleozoic	-	3.5
T4	Paleozoic materials	-	0.04
T5	Faults	-	0.02

ZONE	DESCRIPTION	RECHARGE m <sup>3</sup> y <sup>-1</sup>	
R1	Paleozoic	1.2	
R2	Niebla Fm.	0.3	

**Table 2. Calibrated transmissivity values of the five different materials used in the flow model. Initial reference values from CHG (2012). Recharge values used for the numerical flow model (CHG, 2012).**

The correlation between computed and measured head is shown in Figure 7, which shows an average error lower or equal to 2.5 m. Owing to the highest errors correspond to the most distant areas from the ore deposit, the adjustment was considered acceptable. The mass balance expressed as an annual average value model is shown in Table 3. For a steady-state flow, inputs were equal to outputs.

ZONE	PRESCRIBED HEAD	PRESCRIBED FLOW	LEAKAGE
C1	-1.5	-	-
C2	-	1.2	-
C3	-	0.3	-
C4	-	-	-0.34E-05
FLOW MASS BALANCE ERROR			0.12E-10

**Table 3. Mass balance obtained from the modeling process (m<sup>3</sup>d<sup>-1</sup>). Water inflow is expressed by positive values and negative values instead express water outflow.**

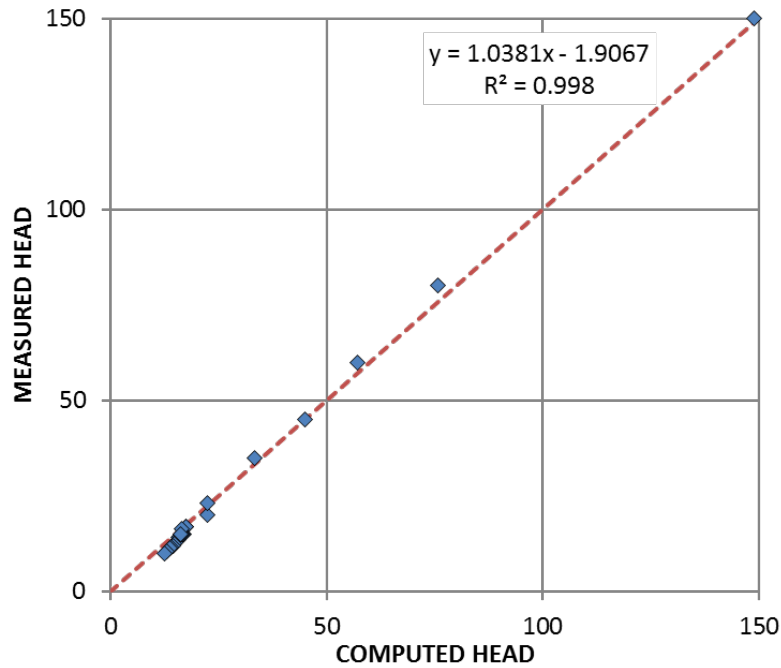


**Figure 7. Correlation between computed and measured hydraulic heads obtained from the flow numerical model.**

The piezometric map of the cross section from NW to SE was thus obtained from the model (Figure 7). As expected, the flow was from the recharge area to SE. There were areas where the flow in the Paleozoic materials had an upward component. This behaviour was mainly detected close to the principal faults where the flow was up to the faults and the groundwater from the Paleozoic discharged to the Niebla aquifer. The main output of the flow modeling was that the unitary flow which circulates upwards through the gossan is  $1.35 \text{ m}^3 \text{ m}^{-2} \text{ y}^{-1}$ . This value was used in the reactive transport model.

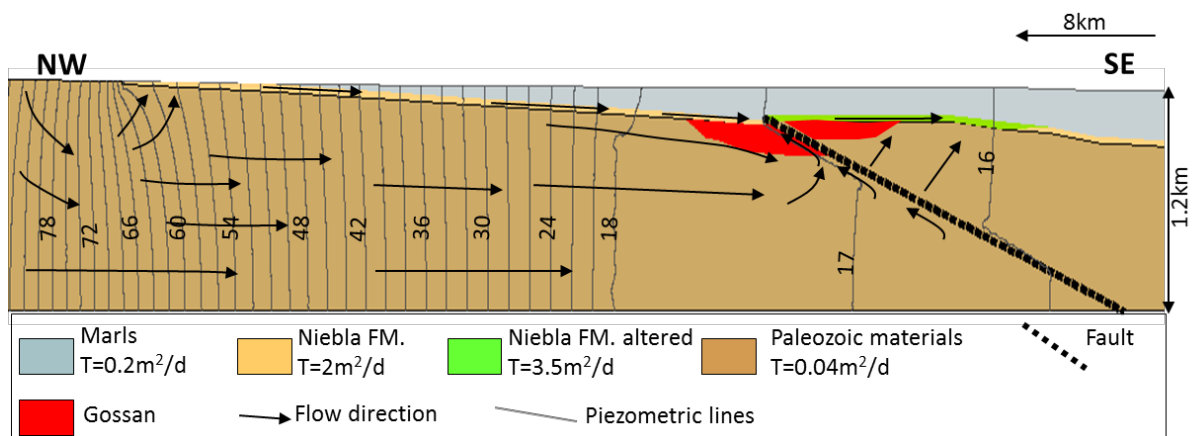




Figure 7. Cross section piezometric map of study area as result of the flow numerical model results. The labels in the isopotential lines correspond to groundwater levels in masl (meters above sea level)

## 3.2. Reactive transport model

### 3.2.1. Initial and boundary conditions

The main goal of this section is to evaluate the feasibility of the conceptual model proposed in section 2 and to estimate the time required for the formation of the siderite rock. Groundwater-mineral interaction was modelled with the computer code RETRASO. This code is based on a full coupling of the multicomponent solute transport equations with chemical reaction equations, either under equilibrium or kinetic laws (Saaltink et al., 1998).

A 1D reactive transport model representing a 10-m long flow line circulating from the base to the top of the gossan was considered. The entire domain was initially composed of goethite (0.7 volume fraction) and refractory silicates (0.1). A porosity of 0.3 has been estimated for the original gossan (Emmons and Laney, 1926; Kelly, 1958). Based on the analysis of goethite, Pb was included in the stoichiometric formula of goethite. However, for the sake of simplicity no Sb and As were included in the calculations. The upstream boundary condition was prescribed flow ( $1.35 \text{ m}^3 \cdot \text{m}^{-2} \cdot \text{y}^{-1}$ ), obtained from the groundwater flow model. The chemical composition of initial and inflow water (Table 4) corresponded to a groundwater composition upstream of the secondary deposit (sample number 5, Figure 2A). The domain was discretized into 20 elements. Calculations were performed at 25°C, the temperature of present day groundwater in the wells close to the deposit.

pH	Ca	DIC	Cl	Fe (II)	Na	S(II)	S(VI)	Pb	DOC
7.8	2.50E-05	6.41E-03	4.47E-02	8.98E-08*	4.63E-02	3.13E-06	1.31E-04	4.84E-09*	2.86E-04

Table 4. Chemical composition of groundwater from the deep aquifer used as initial and inflow water ( $\text{mol} \cdot \text{L}^{-1}$ ). \*Detection Limit.

A total of eleven primary aqueous species, fifteen aqueous complexes and five minerals were selected to describe the geochemical model (Table 5). A summary of all the reactions and kinetic formulations used for the reactive transport model is found in Table 5. Aqueous species were selected from the most abundant species in previous aqueous speciation modeling. Thermodynamic data are those of the Wateq4f database included in the PHREEQC code

(Parkhurst and Appelo, 2013). In addition to initial goethite, neoformed minerals were selected from among the most representative observed in the present-day secondary deposit mineralogy. Mackinawite has been selected as a first step for greigite and smythite formation (Rickard, 2006). Minerals were assumed to precipitate in equilibrium.

PRIMARY AQUEOUS SPECIES	
Ca <sup>+2</sup> , HCO <sub>3</sub> <sup>-</sup> , H <sup>+</sup> , Cl <sup>-</sup> , Fe <sup>+2</sup> , Fe(OH) <sub>3</sub> , Na <sup>+</sup> , HS <sup>-</sup> , SO <sub>4</sub> <sup>-2</sup> , PbCO <sub>3</sub> , CH <sub>2</sub> O	
MINERALS	
Goethite (Fe <sub>0.996</sub> Pb <sub>0.004</sub> OOH), Calcite, Galena, Siderite, Mackinawite	
REACTION	
FORMULATION	
k	
R <sub>1</sub> : Ca <sup>2+</sup> + HCO <sub>3</sub> <sup>-</sup> → CaCO <sub>3</sub> + H <sup>+</sup>	EQUILIBRIUM
R <sub>2</sub> : 2CH <sub>2</sub> O + 4FeOOH + 7H <sup>+</sup> → 4Fe <sup>2+</sup> + HCO <sub>3</sub> <sup>-</sup> + 6H <sub>2</sub> O	r <sub>OM_FeOOH</sub> =k <sub>OM_FeOOH</sub> ·([CH <sub>2</sub> O]/k*+[CH <sub>2</sub> O])·(Ω-1)
R <sub>3</sub> : Pb <sup>2+</sup> + HS <sup>-</sup> → PbS (s) + H <sup>+</sup>	EQUILIBRIUM
R <sub>4</sub> : Fe <sup>2+</sup> + HCO <sub>3</sub> <sup>-</sup> → FeCO <sub>3</sub> + H <sup>+</sup>	EQUILIBRIUM
R <sub>5</sub> : 2CH <sub>2</sub> O + SO <sub>4</sub> <sup>2-</sup> → HS <sup>-</sup> + 2HCO <sub>3</sub> <sup>-</sup> + H <sup>+</sup>	r <sub>OM_SO4</sub> =k <sub>OM_SO4</sub> ·[CH <sub>2</sub> O]·(SO <sub>4</sub> <sup>2-</sup> /kSO <sub>4</sub> + SO <sub>4</sub> <sup>2-</sup> )
R <sub>6</sub> : 1/8H <sub>2</sub> S+FeOOH+1/4H <sup>+</sup> → Fe <sup>2+</sup> +1/8SO <sub>4</sub> <sup>2-</sup> +3/2H <sub>2</sub> O	r <sub>H2S-FeOOH</sub> = k <sub>H2S-FeOOH</sub> ·[H <sub>2</sub> S]
R <sub>7</sub> : Fe <sup>2+</sup> + HS <sup>-</sup> → FeS + H <sup>+</sup>	EQUILIBRIUM

**Table 5. Primary and secondary aqueous species, mineralogical composition and reactions used for the reactive transport model. [1] Liu et al. (2001); [2] Canavan et al. (2006) and [3] Torres et al. (2014).**

Reactions involving organic matter were modelled based on experimental kinetic laws. The reductive dissolution of goethite at the expense of DOC has been investigated by several authors (Torrent et al.,(1987; Schwertmann,1991; Liu et al.,2001; Zachara et al., 2001 and Crosby et al.,2007); however, only a few studies, for example Torrent et al. (1987) and Liu et al. (2001), contain the data necessary to obtain dissolution rates normalized to surface area and can be used in reactive transport modeling. Torrent et al. (1987) measured the goethite reductive dissolution in dithionite and obtained a dissolution rate of 4.6E<sup>-10</sup> mol m<sup>-2</sup>·s<sup>-1</sup>. Liu et al. (2001) performed a comprehensive study of goethite reduction in batch cultures of the groundwater bacterium *Shewanella putrefaciens* at neutral pH. To match the experimental values, they proposed a Monod-type expression where the rate depends on the FeOOH surface and the concentration of lactate used as electron donors and on the thermodynamics of the solution with respect to goethite. In the reactive transport model, the kinetic expression for goethite dissolution proposed by Liu et al. (2001) was used as follows:

$$R = k\sigma \frac{[DOC]}{k^* + [DOC]} (\Omega - 1) \quad (E1)$$

where R is the goethite dissolution rate ( $\text{mol m}^{-3} \text{s}^{-1}$ ), k is the dissolution rate constant ( $\text{mol m}^{-2} \text{s}^{-1}$ ),  $\sigma$  is the specific reactive surface area or the area of water-mineral contact ( $\text{m}^{-2} \text{m}^{-3}$ ),  $k^*$  is an experimental semi-reaction constant with value  $0.52 \text{ mol m}^{-3}$  proposed by Liu et al. (2001), and  $\Omega$  is the saturation of the solution with respect to goethite (ion activity product divided by the equilibrium constant). A value of  $1.38\text{E}^{-10} \text{ mol m}^{-2} \cdot \text{s}^{-1}$  was obtained for k from the initial dissolution experimental values ( $\Omega \ll 1$ ) of Liu et al. (2001). The  $\sigma$  parameter has a large uncertainty that depends on the flow structure. Therefore, a sensitivity analysis of the reactive transport results to this parameter is discussed below. Similar kinetic expressions have also been used to describe the sulfate-reduction at DOC expense (Torres et al., 2014) and the reductive dissolution of goethite by  $\text{H}_2\text{S}$  (Canavan et al., 2006).

### 3.2.2. Results

The results obtained from the reactive transport model show that the goethite dissolution occurred at the expense of organic matter degradation decreased with distance from the inflow because of its consumption along the flow path (Figure 9A and B). Because the rate depends on DOC concentration (equation E1), goethite dissolution also vanished with distance. Goethite dissolution also decreased with time because reactive surface ( $\sigma$  in E1) shrinks with the goethite mass. As observed in Figure 9, most of the siderite with high reactive surface area was replaced in 0.8 Ma. Goethite dissolution released iron and lead to groundwater. Galena and then mackinawite precipitated close to the inflow because of its low solubility product. The  $\text{FeS}$  consumed most of the available  $\text{Fe}^{2+}$ , reducing the precipitation of siderite, which again increased in the second part of the system (Figure 8C, D and E). Calcite did not precipitate in the calculations because of the low concentration of Ca in the inflow groundwater. Porosity was slightly depleted with time in most of the system (Figure 8F) because of the higher molar volume of siderite with respect to goethite and the precipitation of sulfides. However, porosity increased to almost 0.5 of the inflow boundary of the system because no mackinawite formed. A period of 1 Ma was necessary to replace 80% of the goethite initially assumed. By comparing

the flow and goethite dissolution rates, the mass of sulfur carried by groundwater was up to two orders of magnitude higher than that released by goethite dissolution. This explains the heavier values of  $\delta^{34}\text{S}_{\text{SO}_4}$  measured in galena, close to the values of groundwater and far from those of massive sulfides in the IPB (Table 1).

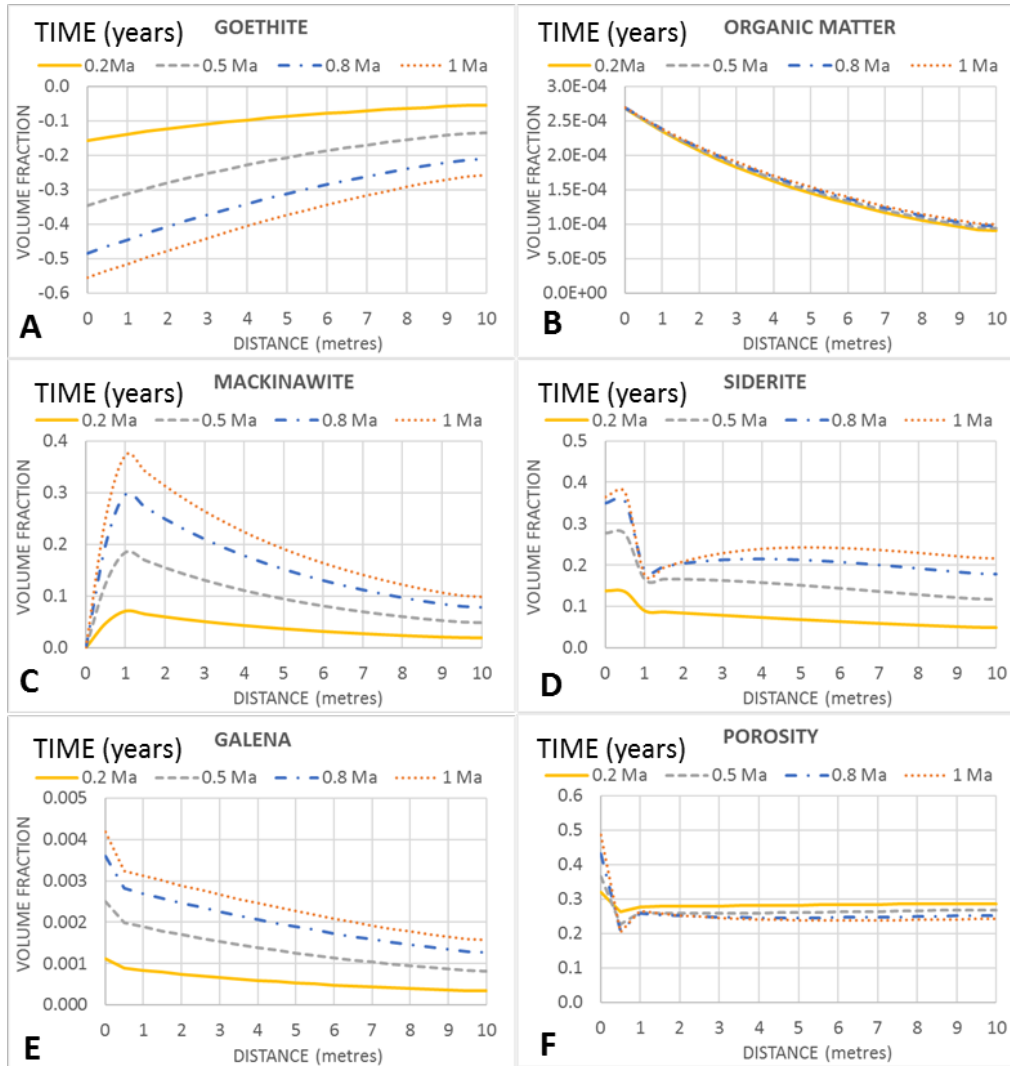


**Figure 8. Results of the reactive transport base model.**

### 3.2.3. Sensitivity analysis

Some of the parameters used in the described calculations (base model) are not well known. Therefore, the impact of changing the values of these parameters on the results was investigated. The reactive surface area, the groundwater flow rate and the DOC concentration in the inflow water have major impacts on the results and were selected for sensitivity analysis. Other parameters, such as the concentration of solutes other than DOC in the inflow water, led to a

slight and expected modification of the results. Thus, the increase of Ca in the inflow water, within the range of the low concentrations measured in groundwater, led to precipitation of minor calcite at the expense of siderite (not represented).

The reactive surface area is the most uncertain parameter in reactive transport modeling because it depends on the structure of the flux (i.e., the wetted surface of the minerals). The value of  $10 \text{ m}^2 \text{ m}^{-3}$  for rock used in the base case corresponds to a flow through fractures separated by 0.20 m. Two more cases with rock reactive surface areas of  $1 \text{ m}^2 \text{ m}^{-3}$ , corresponding to a fracture every 2 m (fracture-controlled flux), and  $50 \text{ m}^2 \text{ m}^{-3}$  rock, corresponding to fractures every 0.04 m (pervasive flux) were tested. The results are plotted in Figure 9. The decrease of the reactive surface area ( $\sigma=1$ ) produced a dramatic decrease in the dissolution of goethite. Consequently, the small amount of  $\text{Fe}^{2+}$  released was precipitated as mackinawite inhibiting the formation of siderite, in clear disagreement with observations. The increase of the reactive surface area ( $\sigma=50$ ) enhanced the goethite dissolution, and the high amount of  $\text{Fe}^{2+}$ ,  $\text{Pb}^{2+}$  and DIC allowed the precipitation of siderite and galena. Porosity was drastically depleted below 0.1 at the end of the system, perhaps modifying the flow structure, as will be discussed below.

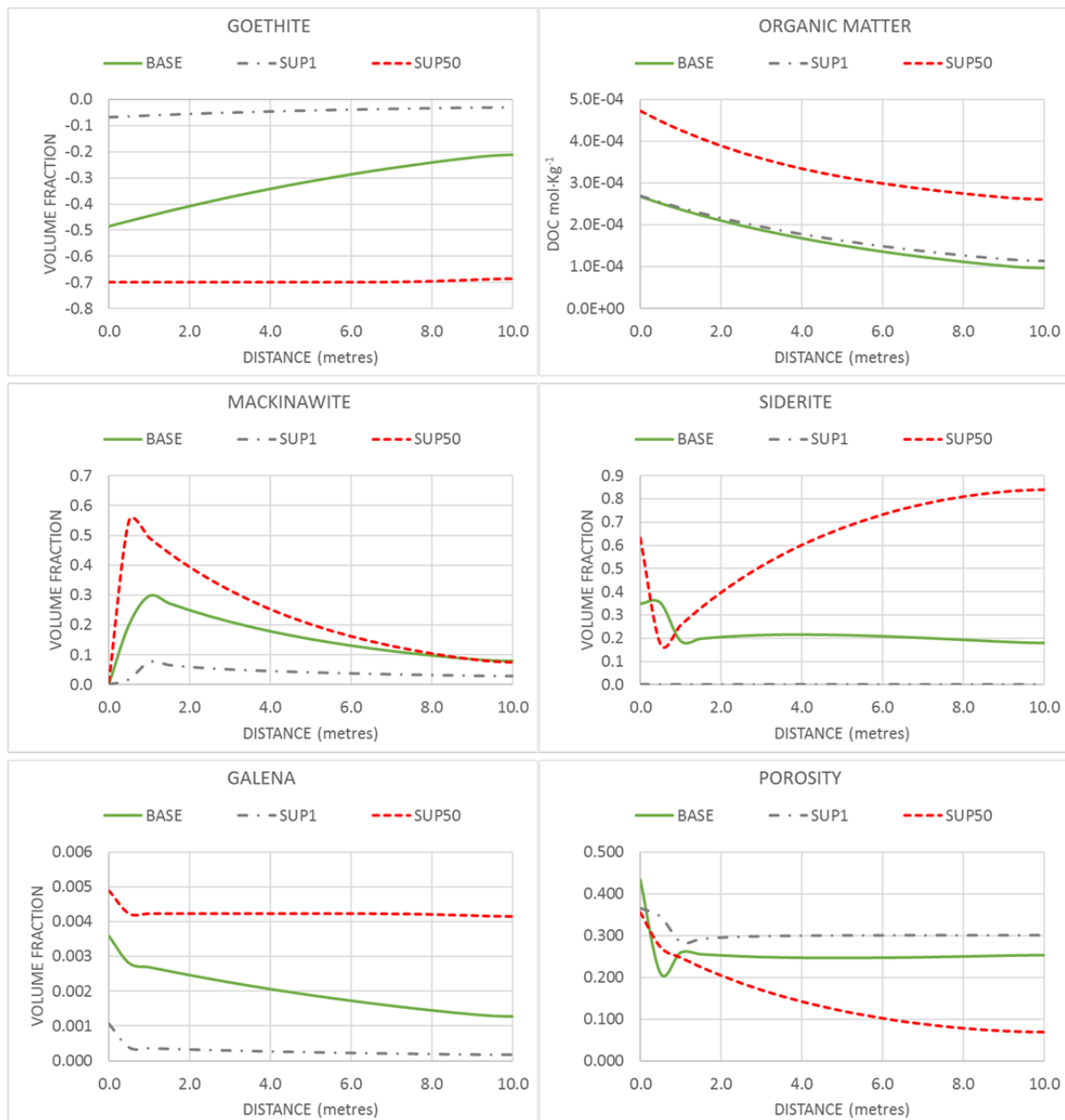


**Figure 90. Sensibility analysis of the reactive transport model based on the specific reactive surface area,  $\sigma_{\text{BASE}}=10 \text{ m}^2 \cdot \text{m}^{-3}$ ,  $\sigma=1 \text{ m}^2 \cdot \text{m}^{-3}$  and  $\sigma=50 \text{ m}^2 \cdot \text{m}^{-3}$  for each mineral. Elapsed time of 0.8 Ma.**

The groundwater flow rate also could have varied in the past with respect to the present-day value. For example, changes in pluviometry or in sea level during the Holocene could have led to changes in groundwater flow. The impact of flows half and twice that of the base case have been tested. The results are plotted in Figure 101.

A flow rate reduction (the flow is divided by two) did not produce major changes with respect to the base model but decreased the galena and mackinawite precipitation because most of sulfur was supplied by groundwater flux. A flow rate increase (double) produced the opposite effect. However, the resulting mineral zonation was similar in all these cases (Figure 10).

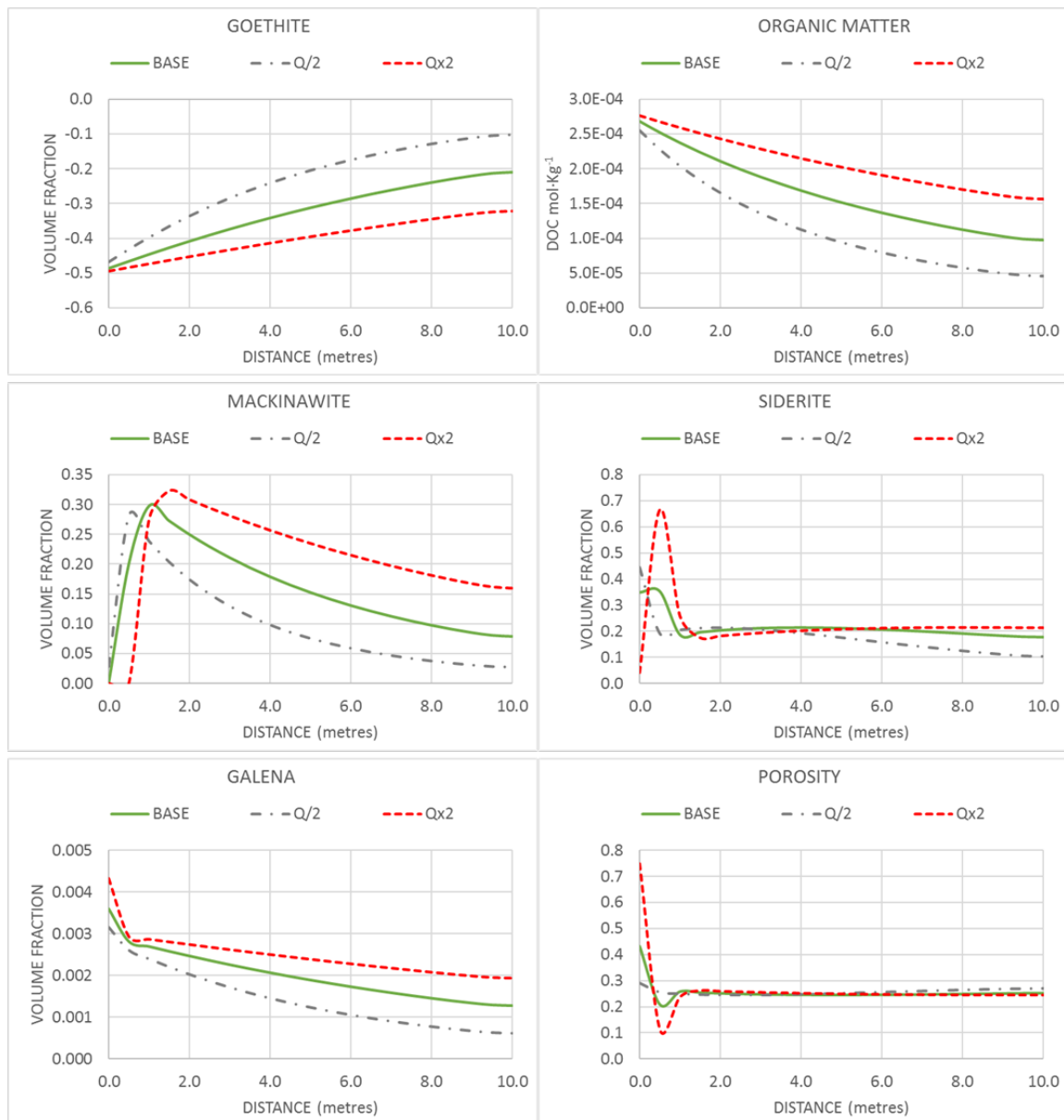
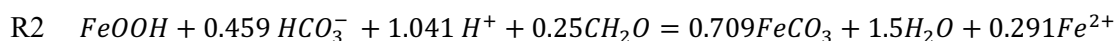


**Figure 10. Sensibility analysis of the reactive transport model based on the flow rate value,  $Q_{BASE}=1.35 \text{ m}^3 \cdot \text{m}^{-2} \cdot \text{y}^{-1}$ ,  $Q/2=0.675 \text{ m}^3 \cdot \text{m}^{-2} \cdot \text{y}^{-1}$  and  $Q \cdot 2=2.7 \text{ m}^3 \cdot \text{m}^{-2} \cdot \text{y}^{-1}$  for each mineral. Elapsed time of 0.8 Ma.**

Finally, DOC concentration from the different wells close to the deposit area displayed a wide range of variation. The impact of the lower and higher DOC concentrations in the results of the model were tested, and the results are plotted in Figure 11. Changes in DOC concentration led to a very distinct results. Indeed, the lower DOC concentration ( $1 \text{ mg} \cdot \text{L}^{-1}$ ) led to a very low amount of goethite dissolution and no precipitation of mackinawite, in disagreement with observations. The higher DOC concentration ( $15 \text{ mg} \cdot \text{L}^{-1}$ ) caused faster goethite dissolution (sulfate reduction rates). Therefore, all the Fe, Pb and DIC released was precipitated as

mackinawite and galena in the first 3 m, and precipitation of siderite was entirely inhibited and delayed to the second 7 m of the system. The complete replacement of goethite occurred in less than 0.8 Ma. Porosity increased to values near 0.5 close to the input, and the formation of the “black rock” formed mainly by sulfides and the “red rock” formed by siderite as described by Tornos et al. (2016) thus became distinct. This result suggests that DOC concentration in past groundwater was probably higher than the average of the values recorded in present day samples.

In the previous calculations, changes in porosity were low and no changes in the hydraulic properties of the rock were assumed. However, the porosity increased up to 0.8 at the inflow in several calculations. The upsurge in porosity could have caused the mechanical collapse of the rock and an apparent increase in deformation at the base of the system, as was described by Yesares et al. (2015). In contrast, in cases of high surface area and/or DOC concentration ( $15 \text{ mg}\cdot\text{L}^{-1}$ ), porosity in the second half of the system approached 0.05. In such a case, reactions leading to an increase in the volume of the solid phase become difficult. Therefore, more realistic modeling would assume that replacement reaction rates are constrained to maintain the solid volume (Ayora et al., 1998), and the following stoichiometry would occur instead of R1:



The resulting model would reduce the siderite precipitated without a virtual decline in porosity (Figure 12). The final resulting texture would be an isomorphic replacement of goethite with siderite, which has been extensively described in Las Cruces siderite rock (Tornos et al., 2016; Yesares et al., 2015).



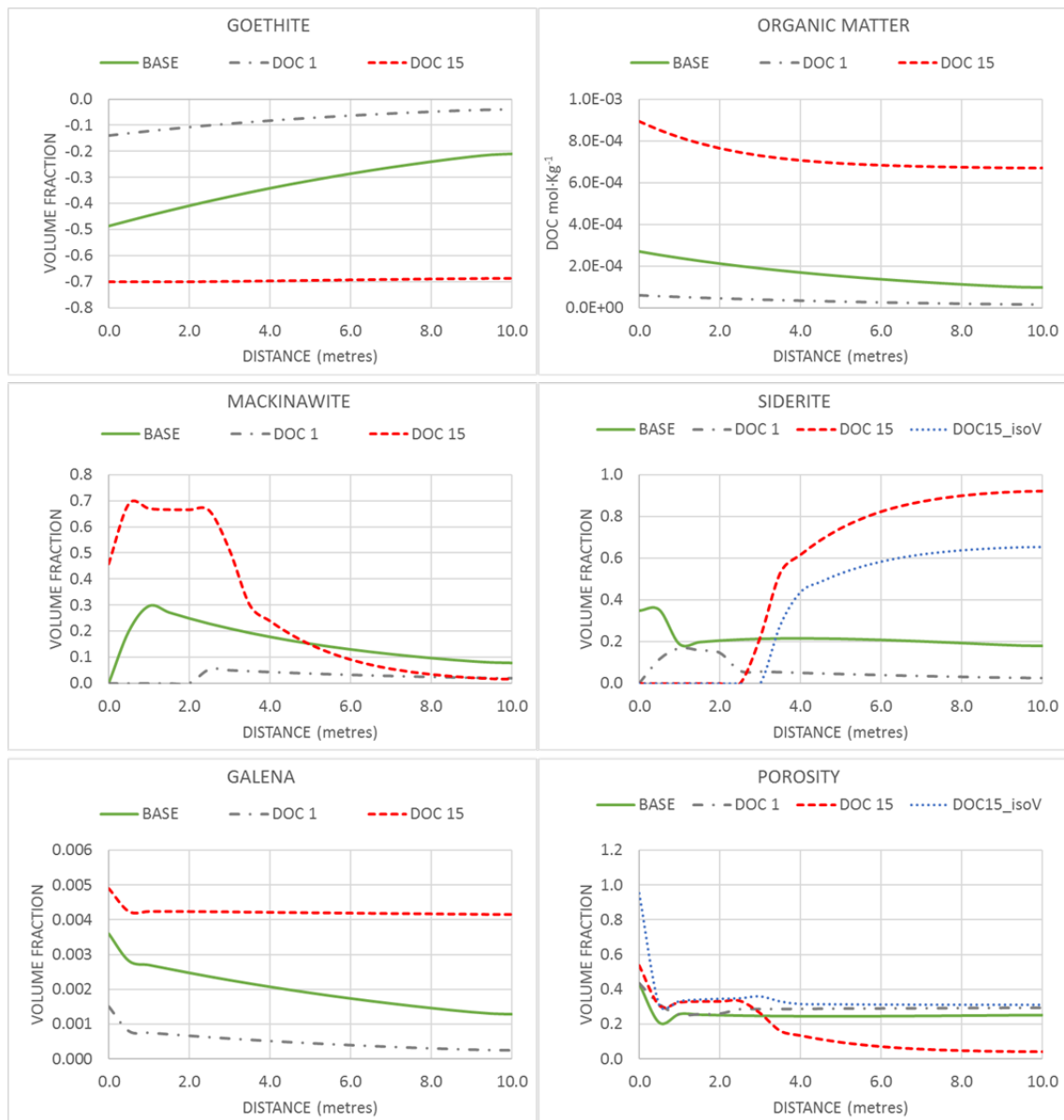


**Figure 11. Sensibility analysis of the reactive transport model based on the organic matter concentration,  $\text{DOC}_{\text{BASE}}=4.5 \text{ mg}\cdot\text{L}^{-1}$ ,  $\text{DOC1} = 1 \text{ mg}\cdot\text{L}^{-1}$  and  $\text{DOC15}=15 \text{ mg}\cdot\text{L}^{-1}$  for each mineral. Elapsed time of 0.8 Ma**

## 4. CONCLUSIONS

This paper quantitatively and qualitatively demonstrated that the reduction of goossan minerals at the expense of the organic matter dissolved in present day groundwater can form the unusual mineralogy of the Las Cruces deposit.

A reactive transport 1D model was developed and applied to calculate the interaction between the present-day groundwater and a goethite goossan. The obtained results show that the goethite dissolution occurs at the expense of organic matter degradation and siderite, galena and iron

sulfides thus precipitate. It required less than 1 Ma to replace the goethite initially assumed. This is consistent with the continuity in the functioning of the hydrogeological system from the lower-Pleistocene (1.8 Ma). The goethite dissolution is the major source of the Pb, As and Sb recorded in galena and of the As found in water from wells. Porosity tends to increase at the inflow boundary and may cause the mechanical collapse of the rock. In the rest of the system, the higher volume of siderite with respect to goethite tends to reduce the porosity. However, volume constraints may induce the observed isomorphic replacement to maintain the porosity and the hydraulic permeability of the final rock. The mass of sulfur carried by groundwater is up to two orders of magnitude higher than that released by goethite dissolution, which explains the high values of  $\delta^{34}\text{S}_{\text{SO}_4}$  values measured in galena, close of those of groundwater.

We concluded from the sensitivity analysis that the groundwater flux was pervasive rather than channelized through fractures. More interestingly, DOC concentration in past groundwater was probably higher than the average of the values recorded in present day samples. Indeed, high DOC concentration produced a mineral zonation formed by Fe-sulfides and siderite that agrees with the observations described by Tornos et al. (2016) of black rock (formed mainly by iron sulfides) and red rock (formed mainly by siderite).

The results from the reactive transport model are also supported by the following evidence observed both in the groundwater and in the rock: (A) low Eh values, the presence of  $\text{H}_2\text{S}$  and the high sulfate isotope values, which indicate that the groundwater has reducing conditions; (B) high ammonium, boron, iodide and dissolved organic carbon (DOC) concentrations together with the low  $\delta^{13}\text{C}$  values for both groundwater and siderite, which shows the important role of the organic matter degradation; and (C) the chemical equilibrium of groundwater with siderite, which indicate the precipitation of this mineral.

## ACKNOWLEDGEMENTS

This work has been supported by Fundación Migres. Other financial support was provided by the Spanish Government project CGL2013-48460-C2-R and the Catalan Government through

the project “Grup de Mineralogia Ambiental i Geoquímica de Fluids” 2014SGR-1456. We would like to thank the Centres Científics i Tecnològics from the Universitat de Barcelona for the isotopic analyses; and Mercè Cabañas, Rafael Bartrolí and Jordi Bellés (IDAEA-CSIC) for chemical analyses. We are also grateful to the staff of Cobre Las Cruces for their collaboration during of fieldwork and granting access to the mine.

## REFERENCES

- Abad de los Santos, F., 2007. La transgresión tortoniense en el margen pasivo de la cuenca del Guadalquivir: respuesta estratigráfica e implicaciones paleontológicas., Universidad de Huelva.
- Almodóvar, G. R., Sáez, R., Pons, J. M., Maestre, A., Toscano, M., & Pascual, E. (1997). Geology and genesis of the Aznalcóllar massive sulphide deposits, Iberian Pyrite Belt, Spain. *Mineralium Deposita*, 33(1-2), 111-136.
- Ayora, C., Taberner, C., Saaltink, M., Carrera, J., 1998. The genesis of dedolomites: a discussion based on reactive transport modeling. *Journal of Hydrology*, 209(1): 346-365.
- Bargar, J., Brown, G., Parks, G., 1997. Surface complexation of Pb (II) at oxide-water interfaces: I. XAFS and bond-valence determination of mononuclear and polynuclear Pb (II) sorption products on aluminum oxides. *Geochimica et Cosmochimica Acta*, 61(13): 2617-2637.
- Belogub, E., Novoselov, C., Spiro, B., Yakovleva, B., 2003. Mineralogical and S isotopic features of the supergene profile of the Zapadno-Ozernoe massive sulphide and Au-bearing gossan deposit, South Urals. *Mineralogical Magazine*, 67(2): 339-354.
- Blake, C., 2008. The mineralogical characterization and interpretation of a precious metal-bearing fossil gossan, Las Cruces, Spain. , Cardiff University, 330 pp pp.
- Bowell, R., 1994. Sorption of arsenic by iron oxides and oxyhydroxides in soils. *Applied Geochemistry*, 9(3): 279-286.
- Canavan, R. W., Slomp, C. P., Jourabchi, P., Van Cappellen, P., Laverman, A. M., & Van den Berg, G. A. (2006). Organic matter mineralization in sediment of a coastal freshwater lake and response to salinization. *Geochimica et Cosmochimica Acta*, 70(11), 2836-2855.
- Capitán Suárez, M.A., 2006. Mineralogía y geoquímica de la alteración superficial de depósitos de sulfuros masivos en la faja piritica ibérica., Universidad de Huelva (UHU), 368 pp.
- Carvalho, D.d., 1976. Considerações sobre o vulcanismo da região de Cercal-Odemira. Suas relações com a faixa piritosa. *Com Serv Geol Portugal*, 60: 215-238.
- Coughlin, B.R., Stone, A.T., 1995. Nonreversible adsorption of divalent metal ions (MnII, CoII, NiII, CuII, and PbII) onto goethite: effects of acidification, FeII addition, and picolinic acid addition. *Environmental science & technology*, 29(9): 2445-2455.
- Crawford, A., Corbett, K., Everard, J., 1992. Geochemistry of the Cambrian volcanic-hosted massive sulfide-rich Mount Read Volcanics, Tasmania, and some tectonic implications. *Economic Geology*, 87(3): 597-619.
- Crosby, H.A., Roden, E.E., Johnson, C.M., Beard, B.L., 2007. The mechanisms of iron isotope fractionation produced during dissimilatory Fe (III) reduction by *Shewanella putrefaciens* and *Geobacter sulfurreducens*. *Geobiology*, 5(2): 169-189.
- CHG, Confederación Hidrográfica del Guadalquivir, 2012. Propuesta de Proyecto de Plan Hidrológico de la Demarcación Hidrográfica del Guadalquivir.
- Davis, J.A., Leckie, J.O., 1978. Effect of adsorbed complexing ligands on trace metal uptake by hydrous oxides. *Environmental science & technology*, 12(12): 1309-1315.
- De Oliveira, D. P. S., Matos, J. X., Rosa, C. J. P., Rosa, D. R. N., Figueiredo, M. O., Silva, T. P., Reiser, F. K. M. (2011). The Lagoa Salgada Orebody, Iberian Pyrite Belt, Portugal. *Economic Geology*, 106(7), 1111-1128.
- Dixit, S., Hering, J.G., 2003. Comparison of arsenic (V) and arsenic (III) sorption onto iron oxide minerals: implications for arsenic mobility. *Environmental science & technology*, 37(18): 4182-4189.
- Doyle, M.G., Allen, R.L., 2003. Subsea-floor replacement in volcanic-hosted massive sulfide deposits. *Ore Geology Reviews*, 23(3): 183-222.
- Emmons, W.H., Laney, F.B., 1926. Geology and ore deposits of the Ducktown mining district, Tennessee. Govt. Print. Off.
- Escudero, R. B. (1994). Cuaternario aluvial dela depresión del Guadalquivir: episodios geomorfológicos y cronología paleomagnética.
- Fendorf, S., Eick, M.J., Grossl, P., Sparks, D.L., 1997. Arsenate and chromate retention mechanisms on goethite. 1. Surface structure. *Environmental science & technology*, 31(2): 315-320.

- Figueiredo, M.-O., Pereira da Silva, T., 2011. The positive environmental contribution of jarosite by retaining lead in acid mine drainage areas. *International journal of environmental research and public health*, 8(5): 1575-1582.
- Forbes, E., Posner, A., Quirk, J., 1976. The specific adsorption of divalent Cd, Co, Cu, Pb, and Zn on goethite. *Journal of soil science*, 27(2): 154-166.
- Galley, A.G., Hannington, M., Jonasson, I., 2007. Volcanogenic massive sulphide deposits. *Mineral deposits of Canada: a synthesis of major deposit-types, district Metallogeny, the evolution of geological provinces, and exploration methods: Geological Association of Canada, Mineral Deposits Division, Special Publication*, 5: 141-161.
- García de Miguel, J., 1990. Mineralogía, paragénesis y sucesión de los sulfuros masivos de la Faja Pirítica en el suroeste de la Península Ibérica. *Boletín Geológico y Minero*, 101(1): 73-105.
- Goldberg, S., Forster, H.S., Heick, E.L., 1993. Boron Adsorption Mechanisms on Oxides, Clay Minerals, and Soils Inferred from Ionic Strength Effects. *Soil Sci. Soc. Am. J.*, 57(3): 704-708.
- Goldberg, S., Johnston, C.T., 2001. Mechanisms of arsenic adsorption on amorphous oxides evaluated using macroscopic measurements, vibrational spectroscopy, and surface complexation modeling. *Journal of colloid and Interface Science*, 234(1): 204-216.
- Hiemstra, T., Van Riemsdijk, W., 1999. Surface structural ion adsorption modeling of competitive binding of oxyanions by metal (hydr) oxides. *Journal of colloid and Interface Science*, 210(1): 182-193.
- Kalbitz, K., Solinger, S., Park, J.-H., Michalzik, B., Matzner, E., 2000. Controls on the dynamics of dissolved organic matter in soils: a review. *Soil Science*, 165(4): 277-304.
- Kase, K., Yamamoto, M., Nakamura, T., Mitsuno, C., 1990. Ore mineralogy and sulfur isotope study of the massive sulfide deposit of Filon Norte, Tharsis Mine, Spain. *Mineral. Deposita*, 25(4): 289-296.
- Kelly, W., 1958. Topical study of lead-zinc gossans. *Bulletin*, 46: 42-47.
- Knight, F., 2000. The mineralogy, geochemistry and genesis of the secondary sulphide mineralisation of the Las Cruces deposit, Spain.
- Kosakevitch, A., Polomero, F., Leca, X., Leistel, J. M., Lenotre, N., Sobol, F. (1993). Contrôles climatique et géomorphologique de la concentration de l'or dans les chapeaux de fer de Rio Tinto (Province Huelva, Espagne). *Comptes rendus de l'Académie des sciences. Série 2, Mécanique, Physique, Chimie, Sciences de l'univers, Sciences de la Terre*, 316(1), 85-90.
- Large, R.R., 1992. Australian volcanic-hosted massive sulfide deposits; features, styles, and genetic models. *Economic Geology*, 87(3): 471-510.
- Leistel, J. M., Marcoux, E., Thiéblemont, D., Quesada, C., Sánchez, A., Almodóvar, G. R., Sáez, R. (1997). The volcanic-hosted massive sulphide deposits of the Iberian Pyrite Belt Review and preface to the Thematic Issue. *Mineralium Deposita*, 33(1-2), 2-30.
- Leuz, A.-K., Mönch, H., Johnson, C.A., 2006. Sorption of Sb (III) and Sb (V) to goethite: influence on Sb (III) oxidation and mobilization. *Environmental science & technology*, 40(23): 7277-7282.
- Liu, C., Kota, S., Zachara, J.M., Fredrickson, J.K., Brinkman, C.K., 2001. Kinetic Analysis of the Bacterial Reduction of Goethite. *Environmental science & technology*, 35(12): 2482-2490.
- Marcoux, E., 1997. Lead isotope systematics of the giant massive sulphide deposits in the Iberian Pyrite Belt. *Mineral. Deposita*, 33(1-2): 45-58.
- Marcoux, E., Moelo, Y., Leistel, J., 1996. Compared ore mineralogy and geochemistry of the massive-sulfide and stringers ore deposits of Southern Spain. *Mineral. Deposita*, 31: 1-26.
- Medina, A.n., Carrera, J., 2003. Geostatistical inversion of coupled problems: dealing with computational burden and different types of data. *Journal of Hydrology*, 281(4): 251-264.
- Miguélez, G., Tornos Arroyo, F., Velasco, F., Videira, J.C., 2011. Geology and Cu Isotope Geochemistry of the Las Cruces Deposits (SW Spain). *Macla* 15: 131-132.
- Moral, F., Balanyá, J. C., Expósito, I., Rodríguez Rodríguez, M., 2013. Análisis geomorfológico de las terrazas fluviales del Bajo Guadalquivir e implicaciones tectónicas.
- Moreno, C., Sáez, R., 1990. Sedimentación marina somera en el Devónico del anticlinorio de Puebla de Guzmán, Faja Pirítica Ibérica. *Geogaceta*, 8: 62-64.
- Moreno C., C.M.A., Doyle M., Nieto J.M., Ruiz F., Sáez R., 2003. Edad mínima del gossan de Las Cruces. *Geogaceta* 33.
- Navarro, A., Fernández, A., Doblas, J.G., 1993. In: IGME (Ed.), *Las aguas subterráneas en España*, pp. 255-256.
- Nickel, E., 1984. The mineralogy and geochemistry of the weathering profile of the Teutonic Bore Cu-Pb-Zn-Ag sulphide deposit. *Journal of Geochemical Exploration*, 22(1): 239-263.
- Nieto, J., Capitán, M., Sáez, R., Almodóvar, G., 2003. Beudantite: a natural sink for As and Pb in sulphide oxidation processes. *Applied Earth Science: Transactions of the Institutions of Mining and Metallurgy: Section B*, 112(3): 293-296.
- Parkhurst, D.L., Appelo, C., 2013. Description of input and examples for PHREEQC version 3: a computer program for speciation, batch-reaction, one-dimensional transport, and inverse geochemical calculations. 2328-7055, US Geological Survey.
- Pascual, E., Sáez, R., Toscano, M., Ruiz de Almodóvar, G., Donaire, T., 1994. Petrología y geoquímica de tobas vítreas del área de Aznalcóllar (Faja Pirítica Ibérica). *Boletín de la Sociedad Española de Mineralogía*, 17(1): 155-156.
- Quesada, C., 1991. Geological constraints on the Paleozoic tectonic evolution of tectonostratigraphic terranes in the Iberian Massif. *Tectonophysics*, 185(3): 225-245.
- Rambaud, F., 1978. Distribución de focos volcánicos y yacimientos en la banda pirítica de Huelva. *Bol. Geol. Min.*, 89: 223-233.

- Rickard, D., 2006. The solubility of FeS. *Geochimica et Cosmochimica Acta*, 70(23): 5779-5789.
- Ross, A.M., 1997. Supergene gold enrichment of the Precambrian aged Flambeau gossan, Flambeau mine, Rusk County, Wisconsin.
- Saaltink, M.W., Ayora, C., Carrera, J. 1998. A mathematical formulation for reactive transport that eliminates mineral concentrations. *Water Resources Research*, 34: 1649-1656.
- Sáez, R., Almodóvar, G., Pascual, E., 1996. Geological constraints on massive sulphide genesis in the Iberian Pyrite Belt. *Ore Geology Reviews*, 11(6): 429-451.
- Salvany, J., Mediavilla, C., Manzano, M., Mantecón, R., 2001. Geología del Valle del Guadiamar y áreas colindantes.
- Scott, K., Ashley, P., Lawie, D., 2001a. The geochemistry, mineralogy and maturity of gossans derived from volcanogenic Zn-Pb-Cu deposits of the eastern Lachlan Fold Belt, NSW, Australia. *Journal of Geochemical Exploration*, 72(3): 169-191.
- Scott, K.M., Ashley, P.M., Lawie, D.C., 2001b. The geochemistry, mineralogy and maturity of gossans derived from volcanogenic Zn-Pb-Cu deposits of the eastern Lachlan Fold Belt, NSW, Australia. *Journal of Geochemical Exploration*, 72(3): 169-191.
- Scheiber, L., Ayora, C., Vázquez-Suñé, E., Cendón, D. I., Soler, A., Baquero, J. C., 2016. Origin of high ammonium, arsenic and boron concentrations in the proximity of a mine: Natural vs. anthropogenic processes. *Science of the Total Environment*, 541, 655-666.
- Scheiber, L., Ayora, C., Vázquez-Suñé, E., Cendón, D. I., Soler, A., Custodio, E., Baquero, J. C., 2015. Recent and old groundwater in the Niebla-Posadas regional aquifer (southern Spain): Implications for its management. *Journal of Hydrology*, 523, 624-635..
- Schermerhorn, L.J.G., 1971. An outline stratigraphy of the Iberian Pyrite Belt. *Boletín Geológico y Minero*, 82(3-4): 239-268.
- Schwertmann, U., 1991. Solubility and dissolution of iron oxides. *Plant and Soil*, 130(1): 1-25.
- Silva, J., Oliveira, J., Ribeiro, A., 1990. South Portuguese Zone. Structural outline. *Pre-Mesozoic Geology of Iberia*, 6(3): 348-363.
- Strauss, G.K., Madel, J., 1974. Geology of massive sulphide deposits in the Spanish-Portuguese Pyrite Belt. *Geologische Rundschau*, 63(1): 191-211.
- Thorner, M., Wildman, J., 1984. Supergene alteration of sulphides, VI. The binding of Cu, Ni, Zn, Co and Pb with gossan (iron-bearing) minerals. *Chemical Geology*, 44(4): 399-434.
- Tighe, M., Lockwood, P., Wilson, S., 2005. Adsorption of antimony (V) by floodplain soils, amorphous iron (III) hydroxide and humic acid. *Journal of Environmental Monitoring*, 7(12): 1177-1185.
- Tornos, F., 2006. Environment of formation and styles of volcanogenic massive sulfides: the Iberian Pyrite Belt. *Ore Geology Reviews*, 28(3): 259-307.
- Tornos, F., 2000. The Iberian Pyrite Belt. R.R. Large, D.J. Blundell (Eds.), *Database on Global VMS Districts, CODES-GEODE*: pp. 19-5.
- Tornos, F., Clavijo, G.E., Spiro, B., 1998. The Filon Norte orebody (Tharsis, Iberian Pyrite Belt): a proximal low-temperature shale-hosted massive sulphide in a thin-skinned tectonic belt. *Mineral. Deposita*, 33(1): 150-169.
- Tornos, F., Velasco, F., Menor-Salván, C., Delgado, A., Slack, J. F., Escobar, J. M., 2014. Formation of recent Pb-Ag-Au mineralization by potential sub-surface microbial activity. *Nature communications*, 5.
- Tornos, F., Velasco, F., Slack, J. F., Delgado, A., Gomez-Miguel, N., Escobar, J. M., Gomez, C., 2016. The high-grade Las Cruces copper deposit, Spain: a product of secondary enrichment in an evolving basin. *Mineralium Deposita*, 1-34.
- Torrent, J., Schwertmann, U., Barron, V., 1987. The reductive dissolution of synthetic goethite and hematite in dithionite. *Clay Miner*, 22(3): 329-337.
- Torres, E., Ayora, C., Jiménez-Arias, J. L., García-Robledo, E., Papaspyrou, S., Corzo, A., 2014. Benthic metal fluxes and sediment diagenesis in a water reservoir affected by acid mine drainage: A laboratory experiment and reactive transport modeling. *Geochimica et Cosmochimica Acta*, 139, 344-361.
- UPC, 2003. Visual Transin code. Universitat Politècnica de Catalunya (UPC).
- Velasco, F., Herrero, J. M., Suárez, S., Yusta, I., Alvaro, A., Tornos, F., 2013. Supergene features and evolution of gossans capping massive sulphide deposits in the Iberian Pyrite Belt. *Ore Geology Reviews*, 53, 181-203.
- Velasco, F., Sánchez-España, J., Boyce, A. J., Fallick, A. E., Sáez, R., Almodóvar, G. R., 1998. A new sulphur isotopic study of some Iberian Pyrite Belt deposits: evidence of a textural control on sulphur isotope composition. *Mineralium Deposita*, 34(1), 4-18.
- Viñals, J., Roca, A., Cruells, M., Núñez, C., 1995. Characterization and cyanidation of Rio Tinto gossan ores. *Canadian metallurgical quarterly*, 34(2): 115-122.
- Whitehead, D., 1974. The sorption of iodide by soil components. *Journal of the Science of Food and Agriculture*, 25(1): 73-79.
- Yesares, L., Sáez, R., Nieto, J.M., de Almodóvar, G.R., Cooper, S., 2014. Supergene enrichment of precious metals by natural amalgamation in the Las Cruces weathering profile (Iberian Pyrite Belt, SW Spain). *Ore Geology Reviews*, 58(0): 14-26.
- Yesares, L., Sáez, R., Nieto, J. M., De Almodovar, G. R., Gómez, C., Escobar, J. M., 2015. The Las Cruces deposit, Iberian Pyrite Belt, Spain. *Ore Geology Reviews*, 66, 25-46.
- Zachara, J.M., Fredrickson, J.K., Smith, S.C., Gassman, P.L., 2001. Solubilization of Fe (III) oxide-bound trace metals by a dissimilatory Fe (III) reducing bacterium. *Geochimica et Cosmochimica Acta*, 65(1): 75-93.



## SUPPLEMENTARY MATERIALS

### Groundwater sampling and analytical procedures

Groundwater samples were collected from a total of 40 wells and piezometers during two field campaigns carried out in February 2012 and September 2013. Wells were purged and samples collected after removing three well volumes or once field parameters had stabilized. The physico-chemical parameters such as temperature ( $^{\circ}\text{C}$ ), pH, Specific Conductance ( $\text{SC}$ ,  $\mu\text{S}\cdot\text{cm}^{-1}$ ), Eh and dissolved oxygen ( $\text{DO}$ ,  $\text{mgL}^{-1}$ ) were measured in situ inside a closed flow cell. Total alkalinity was determined in the field by acid-base titration using an Aquamerck Alkalinity kit.

Groundwater samples for general chemistry were collected in high-density polyethylene, 25 mL bottles for anions and 50 mL for cation-trace samples, previously filtered through a  $0.22\ \mu\text{m}$  nylon filter. Cation-tracer samples were acidified with 1 mL of 20% diluted nitric acid for sample preservation. Anions were analysed by High Performance Liquid Chromatography (HPLC) and cations by Inductively Coupled Plasma Atomic Emission Spectrometry (ICP-AES). The total trace elements concentrations were measured by inductively coupled plasma and mass spectrometry (ICP-MS). In order to differentiate arsenite ( $\text{As (III)}$ ) from arsenate ( $\text{As(V)}$ ) field speciation cartridges were used (Meng et al., 1998). Dissolved Organic Carbon (DOC) samples were collected in 30 mL glass bottles previously muffled. These samples were filtered through a  $0.45\ \mu\text{m}$  and acidified with 1 mL of  $\text{HCl}$  (2N). Bottles were sealed with Parafilm<sup>®</sup> to minimize any contact with air. DOC was analysed by the catalytic oxidation method at  $680\ ^{\circ}\text{C}$  using a Shimadzu TOC-V CSH instrument, with a detection limit of  $0.05\ \text{mg/L}$ .  $\text{NH}_4^+$  and  $\text{I}^-$  concentrations were analysed with ion selective electrodes Orion 9512, with an error of  $\pm 2\%$ .

Twelve samples for  $\text{CH}_4$  and  $\text{H}_2\text{S}$  gas analysis were collected in 250 mL glass bottles with septum cap and stored in an upside-down vertical position according with Capasso and Inguaggiato, (1998). The  $\text{CH}_4$  in the gas phase was determined using a Trace GC Ultra ThermoFisher Scientific chromatograph, with a detection limit of  $0.58\ \text{mg/L}$  and analytical error from  $\pm 0.001$  to  $\pm 0.009\ \text{mg}\cdot\text{L}^{-1}$ . The  $\text{CH}_4$  dissolved in water was calculated by the liquid gas

partition coefficient (Alberto et al., 2000). The  $\text{H}_2\text{S}$  content in the liquid phase was analysed by ionic chromatography with a DIONEX model IC5000, and with a variable wavelength detector with a detection limit of  $0.005 \text{ mg}\cdot\text{L S}_2$  and an analytical error of 5%.

To determine  $\delta^{34}\text{S}$  and  $\delta^{18}\text{O}$  in sulfate, 2L samples in polyethylene terephthalate (PET) bottles were collected, acidified with HCl, with an excess of barium chloride solution added to precipitate  $\text{BaSO}_4$ . The precipitation was carried out at elevated temperature ( $\approx 100^\circ \text{C}$ ) to prevent the formation of  $\text{BaCO}_3$ . After settling, the precipitate was recovered by filtration through a  $3\text{-}\mu\text{m}$  filter and dried at room temperature. The  $\delta^{34}\text{S}_{\text{SO}_4}$  was analyzed in a Carlo Erba Elemental Analyzer (EA) coupled in continuous flow to a Finnigan Delta C IRMS.  $\delta^{18}\text{O}_{\text{SO}_4}$  was analyzed in duplicate with a ThermoQuest TC/EA unit (high temperature conversion elemental analyzer) with a Finnigan Matt Delta C IRMS. The analytical error is 0.1 to 0.6 for  $\delta^{34}\text{S}$  and 0.1 to 0.8 for  $\delta^{18}\text{O}$ .

The samples for  $\delta^{15}\text{N}_{\text{NH}_4^+}$  were collected in high-density polyethylene bottles of 250 mL capacity, previously filtered through a  $0.22 \mu\text{m}$  nylon filter and preserved by adding  $\text{H}_2\text{SO}_4$  (10%) to keep pH below 5.5. At the laboratory, over the water sample a filter-pack is placed by the ammonia trap. Filter-packs consist a 1 cm-diameter GF/D filter (WHATMAN) acidified with  $30 \mu\text{L}$  of  $8\text{N H}_2\text{SO}_4$ , sandwiched between two 2.5 cm diameter  $10 \mu\text{m}$  pore-size Teflon membranes. Two mL of  $\text{Na}(\text{OH})$  5N solution was added in order to increase pH to a value above 12 pH units causing  $\text{NH}_4^+$  to convert to  $\text{NH}_3$ . The bottle was quickly sealed and placed in an orbital shaker during 7 days at room temperature in order to favour the  $\text{NH}_3$  diffusion into the headspace.  $\text{NH}_3$  was then trapped into the filter and converted to  $(\text{NH}_4^+)_2 \text{SO}_4$ . After one week, the filter-pack was placed in an acid-washed glass bottle and placed in a freezer-drier during 2 hours to remove any water from the filter. Then the GF/D filter was removed, placed in a silver-cup and analyzed immediately in an EA-IRMS. The  $\delta^{15}\text{N}_{\text{NH}_4^+}$  were analysed by a diffusion method based on protocols by Sebilo et al., (2004) and Holmes et al., (1998).



**758 Rock sampling and analytical procedures**

759 A total of 16 solid samples from Las Cruces replacement deposit have been analysed. The  
760 samples have been selected from boreholes and supplied by the CLC mining company. The  
761 major mineral phases of the solid samples were identified by X-ray diffraction (XRD) using a  
762 Cu-K $\alpha$  radiation source. For  $\delta^{34}\text{S}_{\text{SO}_4}$  rock analysis, was determined from BaSO<sub>4</sub> by an elemental  
763 analyser coupled in continuous flow with a Delta C Finnigan Matt mass spectrometer.

764 Additionally, some samples have been analysed by, electron microprobe (EPMA) using  
765 wavelength dispersive X-ray spectrometry (WDS) and energy dispersive spectrometry (EDS)  
766 for quantify weight percent of Fe, As, Pb, S and Sb in goethite.

767

768

SAMPLE	pH	Eh (mV)	SC ( $\mu$ S/cm)	T (°C)	DOC	Cl	NO <sub>3</sub>	SO <sub>4</sub>	HCO <sub>3</sub>	Ca	K	Mg	Na	NH <sub>4</sub>	I	Br-	Fe	Mn	B	As	$\delta^{13}\text{C}$ (‰)	18O (‰)	34S(‰)	SI FeCO <sub>3</sub>
44	6.9	159	957	22.5	0.38	39.4	0.1	72.6	442.4	97.8	1.4	14.7	30.8	0.5	0.01	0.22	0.4	0.002	0.15	0.0001	-11.44	5.80	4.85	-0.08
42	6.9	306	922	19.8	0.63	15.5	97.2	16	381.3	109	0.1	3.8	14.8	0.1	0.01	0.14	0.4	0.002	0.03	0.0001	-11.9	3.70	6.34	-0.28
40	7.1	163	903	18.6	0.31	19.1	48.1	13.1	268.5	102.7	0.1	2.8	14.6	0.1	0.01	0.09	0.4	0	0.02	0.0001		5.80	0.94	-0.42
43	7.1	234	999	14.7	0	35	41.6	19.6	297.5	118.3	0.1	9.9	14.8	0.2	0.01	0.18	0.4	0.001	0.03	0.0001		5.90	5.45	-0.86
41	6.9	165	1028	19.6	0.54	27.7	47.1	19.9	427.1	120.2	0.1	4.3	15.8	0.1	0.01	0.14	0.4	0.001	0.03	0.0002		5.90	5.84	-0.27
27	7.4	368	607	20.4	0.74	12.6	16.4	17.3	213.6	68.6	1.9	2.3	16.3	0.1	0.01	0.12	0.4	0.001	0.05	0.0002	-10.73	6.80	0.53	-1.23
46	7.2	137	629	21.2	0.66	16.4	24.3	19.4	236.4	68	2.9	6	19.3	0.2	0.01	0.11	0.4	0.002	0.02	0	-10.02	6.30	-5.58	-1.75
32	7.1	222	916	19.8	0.35	24.7	44.6	30.9	236.4	98.7	4.7	4	17	0.2	0.01	0.12	0.4	0.003	0.06	0.0005		6.87	-8.17	-0.48
24	7.3	-25	491	21.3	3.32	38.9	0.1	13.2	292.6	58.4	5.2	7.4	33.7	0.04	0.02	0.1	0.006	0.01	0.06	0.0008	-11.2	18.10	7.22	-0.89
1	8.4		1015	28.1	4.94	80.3	0.1	0.1	548.7	1.6	3.3	0.5	216	2.57	0.04	0.1	0.005	0.002	0.91	0		9.30	-8.88	-1.88
11	7.5	-200	578	23.3	4.64	71.1	0.1	18.6	243.8	49	3.5	15	49.5	0.79	0.02	5.25	0.005	0.014	0.18	0.0009	-10.09	13.40	-4.80	-2
29	7.4		837	25.1	0.23	44.4	0.1	14.4	308.1	33.7	3.9	12.5	77.6	1	0.03	0.23	0.4	0.031	0.23	0.0015	-5.57	14.47	-6.93	-1.88
17	7.7	-50	812	24.3	4.5	128.6	0.1	10.9	317	32	5.4	8.2	122.7	1.08	0.04	0.38	0.002	0.035	0.45	0.0016	-11.05	6.70	-3.95	-0.41
25	7		4200	21.7	4.73	915.6	13.4	75.4	201.5	177	4.1	50.6	279.3	0.04	0.03	0.1	0.006	0.003	0.47	0.0017	-10.08			-2.32
10	8.2	-297	388	22.6	4.6	43.9	0.1	0.1	158.5	29	2.4	11.9	34.3	0.31	0.03	0.46	0.006	0.013	0.1	0.0025	-10.69	9.21	4.93	-1.56
19	8		989	21.7	4.44	155	9.2	38	317	144.7	5.1	16.5	43.3	0.12	0.01	0.1	0.004	0.012	0.13	0.0097				0.7
22	10.3		943	23.5	7.56	148.4	0.1	0.1	182.9	0.9	3.4	0	163.1	1.7	0.14	0.35	0.005	0	1.49	0.012		16.87	10.53	-6.36
28	8.7	30	1846	27	0.66	198.6	0.1	5.8	328.6	2.1	3.9	0.1	247.3	3.4	0.08	0.81	0.4	0.01	0.61	0.0005	-6.16			-0.76
4	8.6	169	1006	31.7	4.88	110.6	0.1	0.1	475.5	1.7	3.2	0.4	208.2	2.68	0.06	0.1	0.012	0.002	0.76	0.0005	-8.09	18.10	7.22	-1.82
33	8.9		1441	21.8	0.32	91.4	0.1	10.4	570.9	1	3.4	0.1	255.7	2.8	0.04	0.42	0.4	0.003	0.93	0.0006		16.70	1.29	-2.34
13	8.3		1275	26.6	7.83	212.2	0.1	7.2	390.2	2.2	3.7	0.6	246.8	2.35	0.08	0.56	0.006	0.001	1.01	0.0006	-8.81	13.50	-4.39	-1.46
30	7.4	65	834	25.6	0.36	36	0.1	14.7	308.1	35.9	3.9	12.5	71.3	1.1	0.03	0.2	0.4	0.049	0.16	0.0011	-3.8			-0.03
7	8.4		1491	29.2	4.16	305.8	0.1	0.1	317	4	4.5	0.9	277.7	3.23	0.1	0.93	0.006	0.006	0.79	0.0015		17.30	4.92	0.15
35	9		1397	27.8	0.79	97.1	0.1	9	401.2	1	3.3	0.1	221.1	2.7	0.06	0.45	0.888	0.003	0.77	0.0021	-7.57	16.30	9.44	0.16
36	8.6	17	1889	28.2	0.26	238	0.1	6.9	305.1	2.6	4	0.1	273.1	2.8	0.1	0.86	0.4	0.005	0.63	0.0024	-7.44			-0.09
23	8.4		2360	24.4	7.14	522.6	0.1	0.1	304.8	7.6	7	1.7	422.4	4.18	0.2	1.51	0.009	0.036	1.59	0.0025		7.65	-4.27	-0.3
20	8	-130	1499	26	4.75	276.4	0.1	5.8	426.7	13.3	4.4	4.1	271.3	1.91	0.19	0.92	0.002	0.016	1.22	0.006	-10.81			1.14
38	8.4	-24	1973	26.7	0.26	233.1	0.1	0.1	442.4	2.4	4.4	0.1	310.8	2.9	0.15	0.94	0.4	0.005	1.48	0.0079				0.95
34	8.3		2326	29.3	1.32	459.9	0.1	2.1	457.6	3	6.3	0.1	475.9	4.2	0.18	1.76	0.4	0.006	1.7	0.0083				1.25
26	7.5		987	26.5	15.89	151.4	0.1	0.1	365.8	63.7	3.7	7.1	123	5.04	0.13	0.1	0.007	0.159	0.75	0.0011				1.01
18	10.1		2750	27.5	9.76	625.3	8.4	6.3	548.7	1	7.2	0.1	525.2	8.88	0.34	0.4	0.025	0	3.15	0.0014				0.39
3	8.3	-97	2510	31.8	4.5	589.1	0.1	0.1	402.4	5.1	6.5	2.1	469.1	4.7	0.2	1.14	0.023	0.011	1.64	0.0016	-9.27			1
16	10.6		2420	25.5	7.83	503.3	0.1	0.1	353.6	0.6	5.6	0	464.4	12.82	0.49	0.69	0.035	0	3.48	0.0024				-0.48
12	8	-270	2390	32.5	2.86	534.6	0.1	0.1	487.7	5.1	5.6	1.9	442.2	4.58	0.19	0.82	0.02	0.005	2.42	0.0025	-7.58			-0.27
9	8	-128	2400	32.5	5.58	574.2	0.1	0.1	414.5	5.5	6.1	2.2	451.7	4.7	0.17	0.63	0.036	0.007	2.21	0.0039	-8.94	11.41	4.44	-0.32
21	7.9	-190	2880	31.9	5.5	669.3	10.5	10.1	463.3	14	9.2	5.4	510.1	4.64	0.24	1.99	0.03	0.005	2.31	0.005	-10.84			-0.35
2	7.8		2080	28.7	4.75	460.5	0.1	0.1	365.8	5.1	10.1	2.7	378.9	3.25	0.13	1.11	0.137	0.009	1.86	0.0052				-0.32
8	7.7	-290	2670	35.3	5.45	624.6	0.1	0.1	524.3	12.8	8.7	5.1	484.1	4.72	0.26	1.35	0.016	0.012	2.22	0.0121	-10.71			-0.29
5	7.8	-240	5940	37.5	4.57	1581	16.7	12.5	390.2	1	15	30.1	1061	7.49	0.67	4.95	0.005	0.112	2.2	0.0138		10.90	20.38	0.01
37	7.5		2714	36.5	0.49	538.4	0.1	62.5	440.8	19.1	7.7	3.7	519.7	6.4	0.22	2.17	0.4	0.055	2.24	0.1787	-9.79	-29	-4.9	-0.16

Table A1. Hydrogeochemical variables of groundwater samples (mgL<sup>-1</sup>). The sample number correspond to those in Figure 2.

No.	x	y	z	As	Fe	Cu	Pb	S	Sb	Total
1	19.9524	-21.9243	11.4815	0.2736	94.05	0	0.9198	0.3319	0	95.5754
2	19.9941	-21.8759	11.483	0.2872	94.42	0	0.8467	0.2658	0	95.8198
3	20.0208	-21.8734	11.484	0.337	93.71	0.0038	1.0758	0.2707	0	95.3973
4	19.9641	-21.8448	11.4825	0.2436	90.53	0	1.0248	0.4181	0	92.2166
5	12.3774	-23.2334	11.307	0.4774	93.85	0.0144	1.0342	0.3332	0.1963	95.9055
6	12.3303	-23.2619	11.306	0.3322	94.36	0.0109	0.8443	0.3216	0.1228	95.9919
7	12.403	-23.2634	11.3075	0.4172	93.99	0	1.1	0.3575	0.1722	96.0369
8	12.4043	-22.6191	11.312	0.2966	94.34	0	0.9578	0.3692	0.1336	96.0973
9	12.3238	-22.706	11.3105	0.244	94.43	0	0.7825	0.3076	0.1132	95.8774
10	16.8185	-30.1136	11.3585	0.3178	94.53	0.0078	0.8151	0.3371	0.1653	96.1731
11	17.1125	-26.9192	11.385	0.3714	93.75	0.0034	0.9699	0.3267	0.2094	95.6309
12	17.1399	-26.936	11.3855	0.2993	94.68	0.001	0.704	0.3006	0.0962	96.0812
13	17.0666	-26.9314	11.384	0.3596	93.01	0.0074	0.8845	0.2869	0.3464	94.8949
14	16.8589	-27.199	11.3785	0.237	94.44	0	0.7335	0.2854	0.1043	95.8003
15	16.7922	-27.1545	11.378	0.2572	94.43	0.0006	0.8288	0.329	0.1248	95.9705
16	16.7717	-27.1025	11.378	0.2237	94.48	0.0039	0.7259	0.3445	0.0962	95.8743
17	16.2636	-26.9342	11.3675	0.3192	94.44	0.0008	0.8867	0.2888	0.1724	96.108
18	16.1822	-26.9291	11.3645	0.4105	92.4	0.0037	1.0753	0.4153	0.3537	94.6586
19	16.1364	-26.9474	11.363	0.3386	90.61	0	1.0309	0.3825	0.2509	92.613
20	16.1887	-27.0639	11.363	0.419	87.66	0	0.7263	0.4319	1.54	90.7773
21	16.7817	-27.1288	11.377	0.239	94.79	0.0174	0.7669	0.2968	0.1679	96.2781
22	16.7659	-27.1508	11.3765	0.4269	91.63	0.0077	0.9476	0.4102	0.2546	93.6771
23	20.5537	-17.7164	11.5225	0.3729	93.61	0	1.0445	0.3536	0.1749	95.556
24	20.5332	-17.7289	11.5225	0.5731	93.77	0	1.33	0.4094	0.3284	96.4109
25	20.5061	-17.7421	11.521	0.6393	93.52	0	1.22	0.3499	0.3559	96.0852
26	20.4905	-17.7529	11.521	0.3257	94.48	0	0.9278	0.3484	0.1777	96.2597
27	20.469	-17.7633	11.52	0.4551	94	0	1.13	0.3652	0.2311	96.1814
28	21.3781	-16.7883	11.5465	0.4157	93.38	0.0422	1.09	0.3566	0.262	95.5465
29	21.3615	-16.7985	11.546	0.3528	94.4	0	0.9099	0.288	0.1445	96.0953
30	21.3414	-16.8048	11.545	0.3307	94.31	0.0066	0.8655	0.2994	0.1942	96.0065
31	21.3008	-16.8087	11.544	0.3276	94.49	0.0088	0.8338	0.2771	0.1216	96.0589
32	21.5717	-16.9121	11.5505	0.2588	92.16	0	0.9688	0.3878	0.2043	93.9798
33	21.5726	-16.9189	11.5485	0.3044	92.76	0.0027	1.0604	0.3804	0.1878	94.6958
34	21.5705	-16.9268	11.549	0.2592	93.17	0.0083	0.9217	0.3715	0.1307	94.8615
35	21.5645	-16.9462	11.549	0.1934	93.37	0.0143	0.7895	0.4046	0.0807	94.8526
36	10.6006	-17.2541	11.307	0.0981	92.55	0.04	0.7609	0.4584	0.1391	94.0466
37	10.6	-17.245	11.3075	0.2723	92.4	0.0579	0.8196	0.5854	0.1618	94.2971
38	10.6013	-17.2367	11.307	0.3631	93.86	0.0203	0.8488	0.3285	0.1463	95.5671
39	10.598	-17.225	11.307	0.2733	94.07	0.0057	0.8206	0.2748	0.1526	95.5971
40	10.6784	-17.3013	11.3085	0.434	93.75	0	0.8366	0.3497	0.1284	95.4988
41	10.8161	-17.3251	11.311	0.506	92.67	0.0089	1.13	0.4554	0.2584	95.0287
42	10.7937	-17.2978	11.3105	0.4094	91.69	0.0022	1.15	0.5069	0.3663	94.1249
43	10.7906	-17.2943	11.3105	0.484	91.53	0.0051	1.16	0.4851	0.3953	94.0596
44	10.7651	-17.3062	11.31	0.4769	90.33	0.0136	1.0442	0.548	0.5255	92.9382
45	10.961	-17.2684	11.3145	0.7124	93.95	0.0265	0.87	0.3364	0.2751	96.1705
46	10.9424	-17.2643	11.314	0.6406	93.84	0.0025	0.8774	0.3488	0.2923	96.0017
47	10.9274	-17.2825	11.3135	0.853	93.28	0	0.9503	0.3261	0.4837	95.8932
48	10.9185	-17.3235	11.312	0.6968	94.13	0	0.8617	0.3461	0.3456	96.3802
49	10.9412	-17.3389	11.313	0.7858	93.52	0	1.26	0.4003	0.4989	96.465
50	11.298	-17.2052	11.322	0.3715	91.78	0	1.0334	0.4095	0.2175	93.812
51	11.2673	-17.1774	11.3225	0.3988	90.63	0.0044	0.9866	0.4587	0.2206	92.6992
52	-27.4566	-20.0172	11.224	0.4566	91.52	0	0.9254	0.4573	0.3006	93.6599
53	-27.4803	-20.0756	11.2245	0.4276	90.59	0.0115	1.0615	0.4169	0.3628	92.8703

Table A2. Results of Electron Microprobe Analysis (EPMA). of goethite (wt %) by

770  
771  
772  
773  
774